Journal of Geophysical Research: Atmospheres

RESEARCH ARTICLE
10.1029/2018JD028902

Key Points:
- Cloud property retrievals for partially cloudy pixels can be significantly biased
- Based on simple assumptions, the average of the overcast subpixel reflectance can be estimated for MBL cloud scenes
- The estimations yield retrievals, which are unbiased by the clear-sky component of the pixels

Correspondence to:
F. Werner,
frankw@umbc.edu

Citation:
Werner, F., Zhang, Z., Wind, G., Miller, D. J., Platnick, S., & Di Girolamo, L. (2018). Improving cloud optical property retrievals for partly cloudy pixels using coincident higher-resolution single band measurements: A feasibility study using ASTER observations. *Journal of Geophysical Research: Atmospheres*, *123*, 12,253–12,276. https://doi.org/10.1029/2018JD028902

Received 26 APR 2018
Accepted 26 SEP 2018
Accepted article online 9 OCT 2018
Published online 9 NOV 2018

Improving Cloud Optical Property Retrievals for Partly Cloudy Pixels Using Coincident Higher-Resolution Single Band Measurements: A Feasibility Study Using ASTER Observations

F. Werner[1], Z. Zhang[2], G. Wind[3], D. J. Miller[2], S. Platnick[3], and L. Di Girolamo[4]

[1]Joint Center for Earth Systems Technology, Baltimore, MD, USA, [2]Physics Department, University of Maryland, Baltimore, MD, USA, [3]NASA Goddard Space Flight Center, Greenbelt, MD, USA, [4]Department of Atmospheric Sciences, University of Illinois at Urbana-Champaign, Urbana, IL, USA

Abstract Clear-sky contamination is a challenging and long-lasting problem for cloud optical thickness (τ) and effective droplet radius (r_{eff}) retrievals using passive satellite sensors. This study explores the feasibility of improving both τ and r_{eff} retrievals for partly cloudy (PCL) pixels by using available subpixel samples in a visible to near-infrared band, which many satellite sensors offer. Data are provided by high-resolution reflectance (R) observations and cloud property retrievals by the Advanced Spaceborne Thermal Emission and Reflection Radiometer (ASTER) at horizontal resolutions between 30-960m. For partly cloudy 960-m observations, the clear-sky component of the pixels induces significant underestimations of up to 58% for τ, while overestimations in r_{eff} can exceed 41%. This yields underestimations in the derived liquid water path and cloud droplet number concentration of up to 68% and 72%, respectively. By means of three different assumptions it is shown that subpixel R observations in the visible to near-infrared band can be used to estimate higher-resolution R for the second band in the retrieval scheme, as well as the subpixel cloud cover. The estimated values compare well to actually observed ASTER results and are used to retrieve cloud properties, which are unbiased by the clear-sky component of PCL pixels. While the presented retrieval approach is only evaluated for marine boundary layer clouds, it is computationally efficient and can be easily applied to observations from different imagers. As an example, the PCL retrieval scheme is applied to data by the Moderate Resolution Imaging Spectroradiometer, where similar biases for PCL pixels are observed.

Plain Language Summary Clear-sky contamination is a challenging and long-lasting problem for cloud optical thickness and effective droplet radius retrievals using passive satellite sensors. This study explores the feasibility of improving both retrievals for partly cloudy (PCL) pixels by using available subpixel samples in a visible to near-infrared band, which many satellite sensors offer. For partly cloudy 960-m observations, the clear-sky component of the pixels induces significant underestimations of up to −58% for the cloud optical thickness, while overestimations in the effective droplet radius can exceed 41%. This yields underestimations in the derived liquid water path and cloud droplet number concentration of up to 68% and 72%, respectively. It is shown that subpixel reflectance observations in the visible to near-infrared band can be used to retrieve cloud properties, which are unbiased by the clear-sky component of the PCL pixels. While the presented retrieval approach is only evaluated for marine boundary layer clouds, it is computationally efficient and can be easily applied to observations from different imagers. As an example, the PCL retrieval scheme is applied to data by the Moderate Resolution Imaging Spectroradiometer, where similar biases for PCL pixels are observed.

1. Introduction

Marine boundary layer (MBL) clouds cover a majority of the Earth's surface (King et al., 2013; Wood, 2012). They are characterized by an overall negative net radiative forcing (solar plus terrestrial), which implies a cooling effect (Albrecht, 1989; Klein & Hartmann, 1993; Warren et al., 1988). Since these low-level clouds are situated in the boundary layer, their optical and microphysical properties, as well as the solar radiation reflected by these cloud layers, are particularly sensitive to aerosol particle properties such as the particle number concentration

or particle size. Thus, MBL clouds are regularly the focus of aerosol-cloud-interaction studies, including the first (Ackerman et al., 2000; Twomey, 1977; Werner et al., 2014) and second indirect aerosol effects (Albrecht, 1989; Seifert et al., 2015). Moreover, shallow cumulus convection plays an essential role in the transport of moisture, momentum, and heat into the free troposphere (Tiedtke, 1989). Global cloud property observations, such as τ, r_{eff}, liquid water path (*LWP*) and cloud droplet number concentration (*N*), from satellite sensors are indispensable to quantify the role of MBL clouds in the climate system and improve their representation in climate models.

Currently, the most widely used satellite-based remote sensing product of cloud properties is provided by the Moderate Resolution Imaging Spectroradiometer (MODIS) imager aboard the National Aeronautics and Space Administration's Terra and Aqua satellites. The MODIS retrieval algorithm uses *R* from a nonabsorbing (in the visible to near-infrared, VNIR) and absorbing (in the shortwave-infrared, SWIR) spectral band to retrieve τ and r_{eff} via the bispectral solar reflective method (Nakajima & King, 1990; Nakajima et al., 1991; Twomey & Seton, 1980). While the respective MODIS *R* are observed at 250 and 500 m, these observations are aggregated and the cloud products are subsequently derived at a horizontal resolution of 1,000 m. Macrophysical properties of MBL clouds depend on the meteorological regime. Trade wind cumuli , which are ubiquitous over the tropical and subtropical oceans (Siebert et al., 2013), typically exhibit horizontal scales $< 1,000$ m (Norris, 1999; Zhao & Di Girolamo, 2007). Meanwhile, stratocumulus layers, despite their often homogeneous appearances, are composed of small cellular convective eddies driven by longwave cooling and precipitation (Feingold et al., 2010; Wood & Hartmann, 2006). In addition, pockets of open cells are often observed within otherwise overcast cloud decks (Stevens et al., 2005; Wood et al., 2008). As a result, MODIS observations (or those from similar satellite imagers) over broken cumuli and the edges of cumulus and stratocumulus fields inevitably sample partially cloudy (PCL) pixels, which are notoriously challenging for cloud remote sensing. While the operational MODIS collection 6 (C6) product attempts retrievals on the PCL population, the results are reported in a separate data set, because of their lower expected quality. Apart from a bias in retrieved τ and r_{eff}, which subsequently impacts the estimates of aerosol indirect effects, the cloud property retrieval is known to fail regularly. A study of global retrieval failure rates for marine liquid phase clouds by Cho et al. (2015), using MODIS C6 cloud products for the year 2007, concluded that about 33.81% of retrievals fail (for SWIR observations centered around a wavelength $\lambda = 2.1$ μm). This is due to the fact that the sampled SWIR reflectances fall outside the precomputed lookup tables (LUTs) and the sensitivity toward r_{eff} is lost. However, that study also reported that PCL pixels account for about 30% of the studied population. Thus, simply omitting PCL pixels (and thus sub-1,000-m clouds) from the observational data set may lead to a significant sampling bias.

Approaches to retrieve MBL cloud properties for PCL pixels have been discussed by Arking and Childs (1985) and Coakley et al. (2005). The proposed methods determine the cloud properties of the cloudy part of PCL pixels by means of an iterative retrieval scheme, where the average clear-sky *R* and brightness temperatures of the closest overcast and clear pixels are used to estimate the subpixel cloud fraction. Studies using this retrieval scheme are very successful in demonstrating the impacts of surface contamination on satellite retrievals of PCL pixels (Boeke et al., 2016; Coakley et al., 2005; Han et al., 1994; Hayes et al., 2010). However, they share several important limitations: (i) The retrieval assumes a single cloud layer in the subregion in order to derive average cloud top altitudes and associated brightness temperatures for each cloudy cluster. This may induce significant uncertainties in the estimated subpixel cloud fractions. (ii) The approach makes no use of sampled information at the subpixel scale (e.g., *R* observations at 250 and 500 m for MODIS). (iii) The iterative estimation of subpixel cloud cover and retrieval of τ and r_{eff} is computationally expensive, which makes an application for a large number of scenes, or a potential semioperational implementation, impractical. (iv) Most importantly, no ground truth observations are provided to validate and evaluate the results.

This study uses Advanced Spaceborne Thermal Emission and Reflection Radiometer (ASTER) cloud reflectances, cloud mask information and cloud property retrievals at horizontal scales between 30 and 960 m to (i) quantify the biases in retrieved cloud products for PCL pixels and (ii) facilitate a retrieval for PCL pixels by using observed subpixel reflectances in a VNIR band, which mitigates the impacts of clear-sky contamination. The analysis benefits from the availability of reference retrievals that yield the cloud properties from the overcast part of each PCL pixel. The data set explored in this study consists of 48 MBL cloud scenes, which have been thoroughly characterized and colocated with the operational MODIS C6 cloud products (Werner et al., 2016). This manuscript is structured as follows: an overview of the ASTER data set, the retrieval algorithm, and the cloud masking scheme is given in section 2. A statistical analysis of the frequency of PCL observations,

Table 1
Case Number (C1 – C48) and Sample Date of the 48 MBL Scenes, Which Were Sampled Over the Pacific Ocean Off the Coast of California

#	Date	#	Date	#	Date
1	03/02/2006/ 19:14:44	21	06/25/2004/ 19:10:45	41	10/06/2003/ 19:04:27
2	03/06/2005/ 19:20:37	22	07/04/2007/ 19:09:35	42	10/21/2006/ 19:09:31
3	03/06/2005/ 19:20:46	23	07/04/2007/ 19:10:19	43	10/25/2005/ 19:14:44
4	03/06/2005/ 19:20:55	24	07/04/2007/ 19:10:46	44	10/25/2006/ 18:45:26
5	03/06/2005/ 19:21:04	25	07/11/2007/ 19:16:06	45	10/25/2006/ 18:45:35
6	03/06/2005/ 19:21:13	26	07/20/2007/ 19:10:07	46	10/30/2006/ 19:03:35
7	03/08/2005/ 19:08:35	27	07/20/2007/ 19:10:16	47	12/03/2005/ 19:20:56
8	03/08/2005/ 19:08:44	28	07/20/2007/ 19:10:25	48	12/16/2004/ 19:20:41
9	03/08/2005/ 19:08:53	29	08/18/2006/ 19:09:01		
10	04/19/2006/ 19:14:55	30	08/18/2006/ 19:09:18		
11	04/19/2006/ 19:15:13	31	08/26/2003/ 19:09:37		
12	04/19/2006/ 19:15:22	32	08/26/2003/ 19:09:55		
13	04/19/2006/ 19:15:31	33	08/26/2003/ 19:10:12		
14	05/13/2003/ 19:15:46	34	08/29/2006/ 18:52:02		
15	05/30/2006/ 19:08:57	35	08/29/2006/ 18:52:11		
16	06/02/2007/ 19:09:29	36	09/02/2003/ 19:15:12		
17	06/02/2007/ 19:09:47	37	09/07/2005/ 19:14:31		
18	06/03/2005/ 19:14:42	38	09/07/2005/ 19:14:49		
19	06/10/2005/ 19:20:47	39	09/10/2006/ 19:15:21		
20	06/10/2005/ 19:21:04	40	09/11/2004/ 19:21:08		

*Note.*The date format is MM/DD/YYYY Hour:Minute:Second.

the observed retrieval bias for τ and r_{eff}, and the dependence on subpixel horizontal resolution is given in section 3. Approaches to estimate the subpixel cloud cover and reflectance distribution of the absorbing band for the bispectral solar reflective method are presented in sections 4.1 and 4.2, respectively. These estimates facilitate the proposed retrieval scheme for PCL pixels, which is evaluated in section 4.3. Since *LWP* and *N* can be derived from the retrieved τ and r_{eff}, the performance of the new retrieval approach is compared to the standard retrieval for PCL pixels in section 5. The results are validated by means of a much larger ASTER data set in section 6, which consists of rather complex broken cumulus scenes. To test the application of the proposed PCL retrieval for the MODIS imager, the retrieval scheme is applied to MODIS data in section 7. Finally, a summary and conclusions are given in section 8.

2. ASTER Data

Data in this study are provided by high-resolution ASTER observations over 48 marine altocumulus and broken cumulus scenes, which were sampled over the Pacific Ocean off the Coast of California (covering the area 32.051 – 44.427°N and 125.924 – 117.038°W) between May 2003 and September 2007. These granules, which are listed in Table 1, were manually selected and are characterized by sufficient scene cloud covers and cloud sizes, a large number of colocated ASTER and MODIS pixels with successful cloud property retrievals, and the absence of overlying cirrus, multiple cloud layers, and ice phase. These cloud fields cover most of the τ and r_{eff} solution space, as well as varying solar zenith angles and scene cloud covers (*C*).

The ASTER imaging spectroradiometer aboard the National Aeronautics and Space Administration's Terra satellite samples ≈ 650 scenes daily (mostly over land), with each scene about 60×60 km^2 in area. Information on the ASTER instrument design and technical specifications are reported in Yamaguchi et al. (1993), Yamaguchi et al. (1998), and Abrams (2000). The horizontal resolution of ASTER observations in the VNIR, SWIR, and thermal infrared spectral wavelength range is 15, 30, and 90 m, respectively. From the equations and coefficients in Abrams et al. (2004) ASTER cloud top reflectances (*R*) can be derived from the raw digital counts, which are characterized by an absolute radiometric uncertainties of <4% (Yamaguchi et al., 1998).

Retrieved τ and r_{eff} are provided by an ASTER-specific, research level retrieval algorithm (Werner et al., 2016). This algorithm utilizes the operational MODIS C6 retrieval core (King et al., 1997; Platnick et al., 2003) and yields reliable cloud top, optical and microphysical variables, which compare well with the operational MODIS C6 products (Werner et al., 2016). The retrieval is based on the bispectral solar reflective method, where R at two different wavelengths (λ) are used to simultaneously infer τ and r_{eff} (Nakajima & King, 1990; Nakajima et al., 1991; Twomey & Seton, 1980). This approach utilizes so-called LUTs from one-dimensional (1-D) radiative transfer simulations, that are composed of modeled R over a model cloud for varying τ and r_{eff}, as well as different solar and viewing geometries. For the ASTER cloud property retrieval the observations in the nonabsorbing band are provided by ASTER band 3N (nadir-viewing mode) reflectances centered around $\lambda = 0.86\,\mu m$ in the VNIR ($R_{0.86}$), while the observations in the absorbing band are from ASTER band 5 reflectances centered around $\lambda = 2.1\,\mu m$ in the SWIR ($R_{2.1}$). The mean retrieval uncertainties are estimated to be 15% and 23% for τ and r_{eff}, respectively (Werner et al., 2016). Due to the native resolution of the ASTER SWIR observations, the highest possible horizontal resolution of retrieved τ and r_{eff} is 30 m. However, by aggregating $R_{0.86}$ and $R_{2.1}$ within increasingly larger pixel footprints both cloud variables are available at arbitrary horizontal resolutions. In this study both τ and r_{eff} are derived for horizontal resolutions between 30 and 960 m, which covers the native ASTER and operational MODIS C6 scales. Note that the retrieved τ is scaled to the 0.65 μm band (i.e., band 2).

The distinction between clear-sky and overcast pixels in this study is performed with the cloud conservative cloud masking scheme introduced in Werner et al. (2016). Cloud detection from this algorithm is based on five spectral tests that compare absolute ASTER reflectances, as well as color ratios and a derived brightness temperature, to predefined thresholds. Those thresholds, which were carefully developed and tested on a number of different ASTER data sets, flag each ASTER pixel as either confidently cloudy, probably cloudy, probably clear, or confidently clear (flag values of 0–3, respectively). As illustrated in Werner et al. (2016), the results from this scheme compare well with the operational MODIS cloud mask product for colocated observations, as well as the case-by-case ASTER cloud mask reported in Zhao and Di Girolamo (2006). It is important to note that in this study a binary cloud flag is applied (i.e., cloudy pixels are composed of those with flag values of 0–1, while flag values of 2–3 consequently designate clear pixels).

3. ASTER Observations of Partially Cloudy Pixels

This section provides information about the observed cloud properties of the 48 ASTER scenes. Statistics about the occurrence of PCL pixels are given in section 3.1. The biases in pixel level retrievals of τ and r_{eff}, which are induced by clear-sky contamination on the subpixel scale, are assessed in section 3.2. Finally, a scale analysis with different subpixel horizontal resolutions is presented in section 3.3.

3.1. PCL Statistics

A map of $R_{0.86}$ sampled at a horizontal resolution of 30 m above a small broken cumulus field over the ocean on 3 December 2005 (case 47 in ; Werner et al., 2016) is shown in Figure 1a. This example scene covers an area of about 10×10 km^2 and depicts parts of two convective clouds, as well as some smaller cloudy fragments. At this scale the highly heterogeneous cloud structure becomes obvious and numerous illuminated and shadowed areas are visible. In comparison, at 960-m horizontal resolution most of the fine-scale cloud structures are smoothed out, as illustrated in Figure 1b. Due to the abundance of cloud edges in this scene, there are a multitude of 960-m pixels that are only partially covered with clouds on the subpixel scale. For each of these pixels the subpixel cloud cover (C_{sub}) is calculated from the observed number of cloudy 30-m subpixels, which is determined by the extensive cloud masking scheme described in section 2. Note that at this subpixel scale, there are $32 \times 32 = 1,024$ available subpixels within a 960-m pixel to calculate C_{sub}. Cloudy 30-m pixels for this scene are shown in white color in Figure 1c. Here red boxes indicate cloudy 960-m pixels with a successful τ and r_{eff} retrieval and $C_{sub} < 0.95$, while light green boxes show pixels with $C_{sub} = 0.95 - 1$ (i.e., almost overcast pixels). Since the applied cloud mask is cloud conservative with respect to clouds very thin clouds might be missed by the algorithm, which explains some of the missed cloud detections for very low reflectances. Still, it is obvious that for the example scene in Figure 1 a majority of the cloudy 960-m samples can be considered to be PCL pixels. Even though all pixel outlines in red have a successful cloud property retrieval at a horizontal resolution of 960 m there are a number of observations with very few cloudy subpixels.

Similar analysis has been performed for all 48 ASTER scenes. Figure 2a shows the cumulative probability density function of observed C_{sub} for all cloudy 960-m pixels. As before, only pixels with a successful cloud property

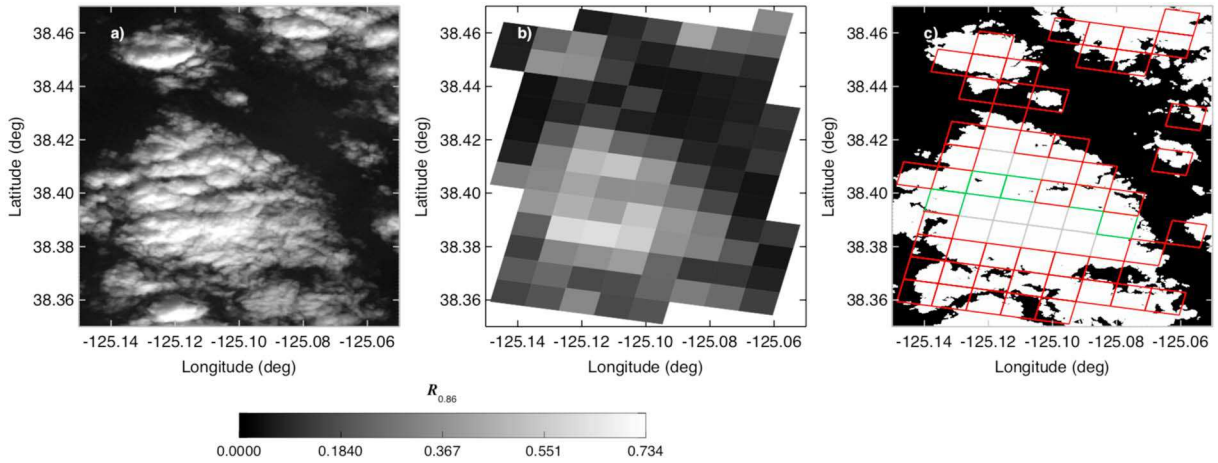

Figure 1. (a) Single band, grayscale image of ASTER band 3N reflectances ($R_{0.86}$) for a scene observed off the coast of California on 3 December 2005 at 19:20:56 UTC. The horizontal resolution is 30 m. (b) Same as (a) but the $R_{0.86}$ sampled at the 30-m scale are aggregated to a horizontal resolution of 960 m. (c) Binary cloud flag based on 30-m ASTER data; white colors indicate cloudy 30-m pixels, based on the cloud masking algorithm described in section 2. Red and light green boxes highlight partially cloudy 960-m pixels with a successful cloud property retrieval, where the subpixel cloud cover (C_{sub}; derived from 30-m data) is in the range of $0 > C_{sub} < 0.95$ and $0.95 > C_{sub} < 1.0$, respectively. Gray boxes indicate overcast 960-m pixels (i.e., $C_{sub} = 1.00$) with a successful cloud property retrieval.

retrieval are considered. Overall, about 28.2% of data points are classified as PCL pixels (i.e., $C_{sub} < 0.95$; 37,164 pixels in total), while 15.7% (20,697), 8.0% (10,463), and 2.4% (3,206) exhibit $C_{sub} < 0.75, 0.5, 0.25$, respectively. This means, that close to 30% of observed pixels are either excluded from standard retrieval approaches or are misrepresented as overcast, which agrees well with the findings of Cho et al. (2015). Figure 2b shows the probability density function (PDF) of C_{sub} for all PCL observations. Clearly, the largest contribution comes from observations with $C_{sub} > 0.95$. These pixels are usually not cloud edge samples, but rather in-cloud observations with low pixel level τ retrievals. Note that a less conservative cloud masking algorithm might classify such pixels as overcast. Apart from $C_{sub} < 0.1$, there are noticeable contributions from the whole C_{sub} range.

The C_{sub} statistics in Figure 2 are derived from ASTER samples at a horizontal resolution of 30 m. However, the analysis in this study covers subpixel horizontal resolutions up to 480 m, with a fixed pixel level horizontal resolution of 960 m. This has a significant impact on C_{sub}, because for subpixel observations at 240 m (480 m) only $4 \times 4 = 16$ ($2 \times 2 = 4$) subpixels are available to calculate C_{sub}. As a result, a 960-m pixel can only exhibit $C_{sub} = 0.00, 0.25, 0.5, 0.75, 1.00$ if calculated from 480-m data. Compared to the 30-m cloud mask, where almost clear and almost overcast pixels are possible (i.e., C_{sub} close to 0 and 1, respectively), such pixels

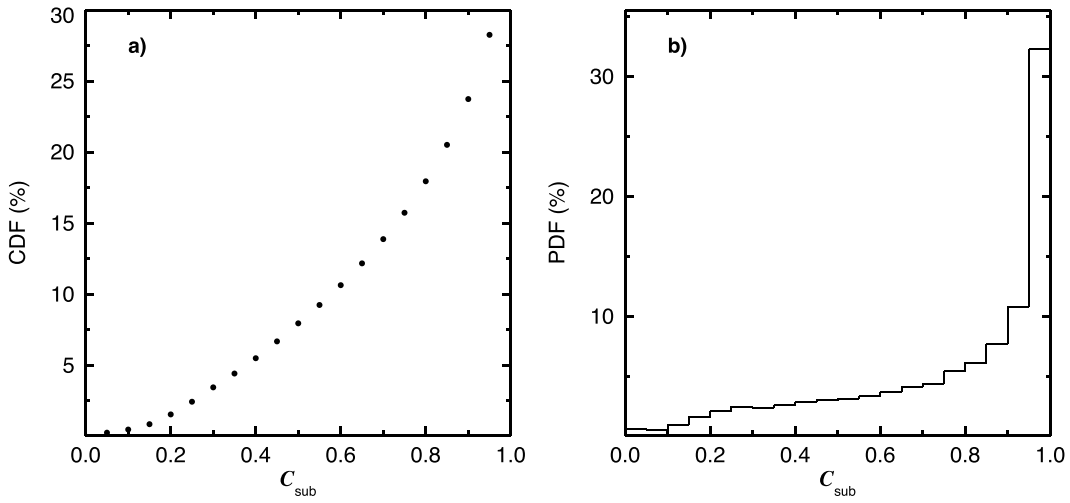

Figure 2. (a) Cumulative density function (CDF) of C_{sub} for all cloudy pixels (for visibility reasons the last data point at 100% is not shown). Data are from 48 altocumulus and broken cumulus scenes sampled off the coast of California. The horizontal resolution at the pixel level is 960 m. (b) Probability density function (PDF) of C_{sub} for all partially cloudy pixels.

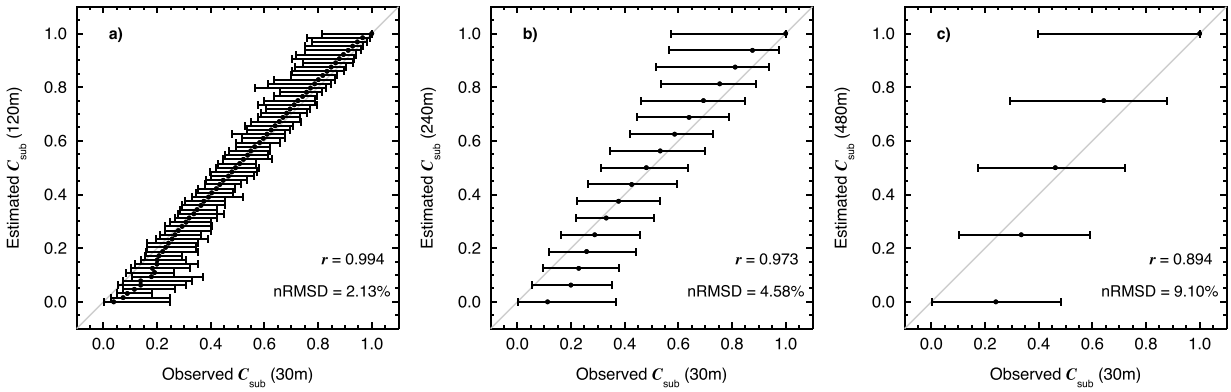

Figure 3. Comparison between subpixel cloud cover (C_{sub}; based on the extensive cloud masking scheme described in section 2) derived from Advanced Spaceborne Thermal Emission and Reflection Radiometer reflectances sampled at a horizontal resolution of 30 m and those from (a) 120-m, (b) 240-m, and (c) 480-m data. The correlation coefficient *r* and normalized root-mean-square deviation (nRMSD) between C_{sub} from 30 m and lower-resolution reflectances is given. The gray diagonal line indicates the identity line.

will either be classified as clear or fully overcast from 480-m subpixel data. This is illustrated in Figures 3a–3c, where the subpixel cloud cover at the native ASTER resolution is statistically compared to C_{sub} based on 120, 240, and 480 − m observations, respectively. The horizontal bars indicate the spread of the 30-m results for each 120, 240, 480 − m C_{sub} bin. For the 120 − m results, the median 30-m cloud mask values (dots) closely follow the identity line and high values of Pearson's product-moment correlation coefficient between the low- and high-resolution C_{sub} are observed ($r = 0.994$). Moreover, the normalized root-mean-square deviation (nRMSD; defined as the RMSD between the two data sets, normalized by the mean 30-m C_{sub}) is 2.13%. Increasing the subpixel horizontal resolution to 240 m (480 m) yields a decreased correlation of $r = 0.973$ (0.894), as well as larger deviations from the 30-m results with nRMSD = 4.58% (nRMSD = 9.10%). Overall, an increase in subpixel horizontal resolution from 30 m to 120, 240, and 480 m results in an increase in average C_{sub} of 0.72%, 1.91%, and 4.34%, respectively.

Note that these statistics are particular to the 48 ASTER scenes in this study. More comprehensive statistics about the scale dependence of cloud fraction estimates are reported by Shenk and Salomonson (1972), Wielicki and Parker (1992), Krijger et al. (2007), Dey et al. (2008), and Ackerman et al. (2008), where the relationships between domain size, pixel resolution, cloudiness, and cloud macrophysical parameters are analyzed for a wide range of observational conditions. However, similar to the comparisons in Figure 3, these studies find a strong dependence of cloud fraction on observational scale, with significant increases in cloud cover with increasing sensor resolution due to PCL pixels being counted as overcast. Thus, in this study PCL pixels (i) are characterized by a successful τ and r_{eff} retrieval at 960-m horizontal resolution, (ii) exhibit $C_{sub} < 1$ at all possible subpixel scales between 30 and 480 m, and (iii) include at least one subpixel with a successful cloud property retrieval. These conditions provide a reliable data set of 10,484 PCL pixels at all scales that avoids almost clear (i.e., very low 30-m C_{sub}; minimum remaining value is $C_{sub} = 0.21$) and almost overcast pixels (i.e., very high 30-m C_{sub}; maximum remaining value is $C_{sub} = 0.88$).

3.2. Retrieval Bias for PCL Pixels

A PCL observation at the pixel level scale consists of both clear-sky subpixel reflectances ($R_{0.86,c}$ and $R_{2.1,c}$; indicated by the index *c*) and overcast subpixel reflectances ($R_{0.86,o}$ and $R_{2.1,o}$; indicated by the index *o*), which are sampled above clouds. These reflectances are connected to the total reflectances at the pixel level scale (the standard $R_{0.86}$ and $R_{2.1}$ samples at, e.g., 960 m) as follows:

$$\begin{aligned} R_{0.86} &= (1 - C_{sub}) \cdot \overline{R_{0.86,c}} + C_{sub} \cdot \overline{R_{0.86,o}} \\ R_{2.1} &= (1 - C_{sub}) \cdot \overline{R_{2.1,c}} + C_{sub} \cdot \overline{R_{2.1,o}}. \end{aligned} \quad (1)$$

Here the horizontal bars above the clear-sky and overcast reflectance indicate the spatial averages of the respective variable. In the case of an overcast pixel, $C_{sub} = 1$ and subsequently $R_{0.86} = \overline{R_{0.86,o}}$ (similarly for $R_{2.1}$). Conversely, for a PCL pixel $C_{sub} < 1$ and, assuming observations above a dark surface (e.g., over oceans), both $R_{0.86} < \overline{R_{0.86,o}}$ and $R_{2.1} < \overline{R_{2.1,o}}$. As a result, for PCL pixels there is a difference between the standard τ and r_{eff}

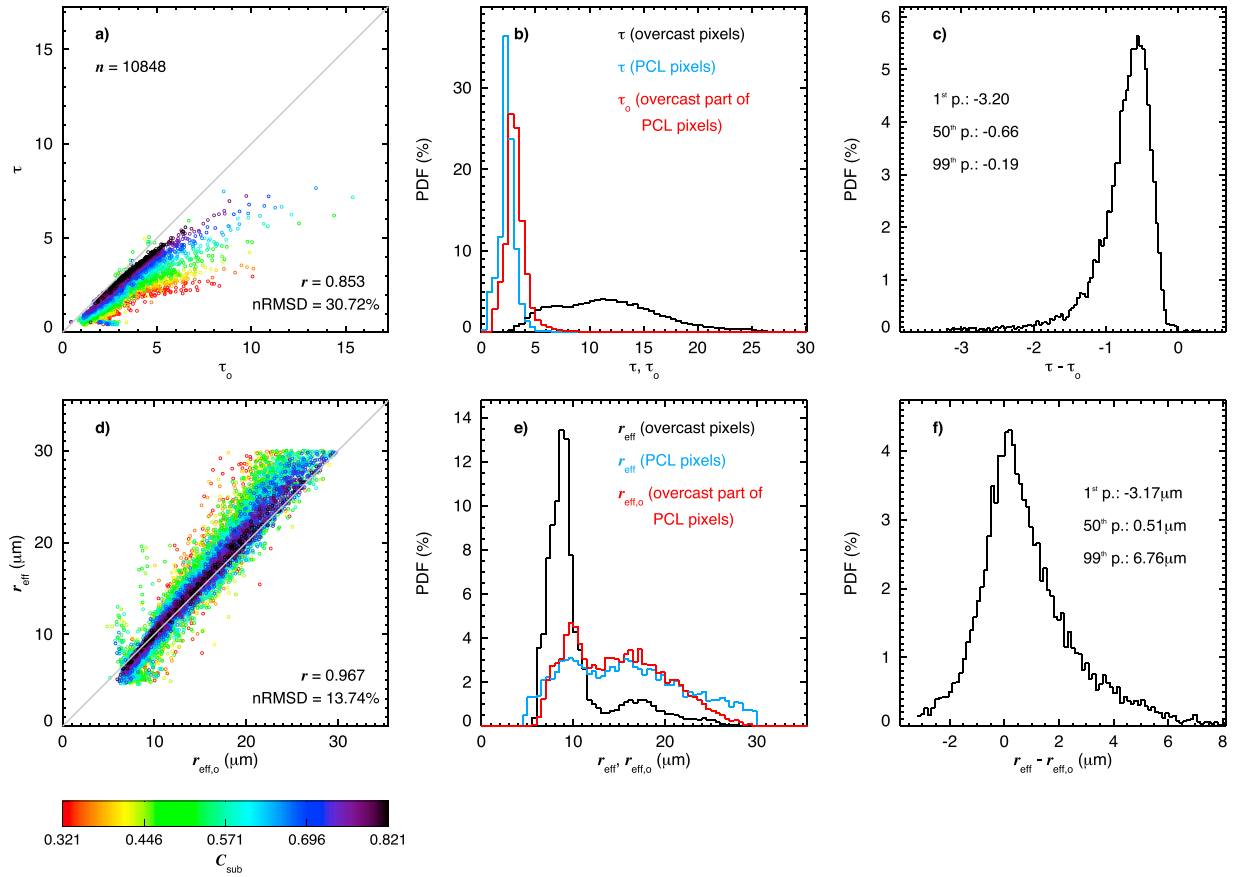

Figure 4. (a) Comparison between retrieved cloud optical thickness based on the average reflectance of the cloudy part of a pixel (τ_o) and the one retrieved from the total reflectance (τ). The pixel level scale is 960 m, while the subpixel data are provided by 30 − m observations. Colors indicate the subpixel cloud cover (C_{sub}; based on the extensive cloud masking scheme described in section 2); the gray diagonal line indicates the identity line. The number of observations (n), correlation coefficient (r), and normalized root-mean-square deviation between τ_o and τ (nRMSD) is given. (b) Probability density functions (PDFs) of τ_o (red) and τ for PCL pixels (blue). Additionally, $\tau = \tau_o$ for overcast pixels is illustrated (black). (c) PDF of the difference between τ and τ_o for all partly cloudy (PCL) pixels. The 1st, 50th, and 99th percentiles are given. (d)–(f) Same as (a)–(c), but for the effective droplet radius ($r_{eff,o}$ and r_{eff}).

retrievals, which are based on the total reflectances $R_{0.86}$ and $R_{2.1}$, and the actual underlying cloud properties τ_o and $r_{eff,o}$ (based on $\overline{R_{0.86,o}}$ and $\overline{R_{2.1,o}}$).

A comparison between τ_o and τ for all PCL observations is shown in the scatter plot in Figure 4a. Colors indicate the value of C_{sub}, with black (red) colors indicating high (low) C_{sub}. Because of the reduced VNIR reflectance for PCL pixels following equation (1), almost all samples are characterized by a strong underestimation of the pixel level τ compared to τ_o. This underestimation becomes more pronounced with decreasing C_{sub}. Even though the correlation coefficient between τ_o and τ is still high ($r = 0.853$), the bias between the two data sets is significant (nRMSD = 30.72%). Rather, similar PDFs of τ_o (red) and τ (blue) for all PCL pixels are illustrated in Figure 4b. There is a shift toward larger values as the 1st, 50th, and 99th percentiles of τ observations change from 0.61, 2.35 and 4.62 to 1.26, 3.05 and 6.95 for τ_o, respectively. Compared to the results for PCL pixels, the cloud optical thickness distribution of all overcast pixels (black), where $C_{sub} = 1$ and $\tau = \tau_o$, shows significantly larger values. While the PCL and overcast distributions are not directly comparable because they are composed of completely different populations, these vastly different τ ranges are not surprising. PCL pixels are usually associated with cloud holes and edges, where turbulent mixing and evaporation processes yield a reduced liquid water amount and geometrical thickness (Schmeissner et al., 2015). A PDF of the difference between τ and τ_o for all PCL pixels is illustrated in Figure 4c; however, although a wider range of $-8.22 < \tau - \tau_o < 0.62$ is observed, only the 1st and 99th percentiles of the difference ($-3.21 < \tau - \tau_o < -0.19$) are shown for visibility reasons. For all analyzed PCL pixels the median underestimation in cloud optical thickness due to clear-sky contamination is −0.66.

Table 2
Comparison Between Pixel Level Retrievals (τ and r_{eff}) and the 30-m Subpixel Cloud Properties (τ_o and $r_{eff,o}$), As Well As Comparisons Between τ_o and $r_{eff,o}$ at Different Horizontal Resolutions

	1st, 50th, 99th percentiles	nRMSD	r
$\tau - \tau_o$ (30 m)	−62.98%, −22.30%, −7.68%	30.72%	0.853
τ_o (240 m) − τ_o (30 m)	−19.74%, −5.99%, 3.73%	8.79%	0.985
τ_o (480 m) − τ_o (30 m)	−36.12%, −10.34%, 10.76%	15.55%	0.941
$r_{eff} - r_{eff,o}$ (30 m)	−34.60%, 3.54%, 38.36%	13.74%	0.967
$r_{eff,o}$ (240 m) − $r_{eff,o}$ (30 m)	−14.24%, −2.53%, 5.51%	4.06%	0.996
$r_{eff,o}$ (480 m) − $r_{eff,o}$ (30 m)	−28.64%, −6.03%, 13.20%	9.26%	0.977

Note. The 1st, 50th, and 99th percentiles of relative biases, the normalized root-mean-square deviations (nRMSD), and the correlation coefficients (r) between the respective variables are given.

Similarly, a comparison between $r_{eff,o}$ and r_{eff} is shown in Figures 4d–4f. While $\tau < \tau_o$ for almost all PCL pixels, both overestimations and underestimations of r_{eff} (compared to $r_{eff,o}$) are observed and the comparison exhibits a higher correlation ($r = 0.967$) and lower nRMSD (13.74%). As before, the deviations between the two retrievals increase with decreasing C_{sub}. The PDF of r_{eff} for PCL pixels is rather flat, as the 1st, 50th, and 99th percentiles of observations are 5.21, 15.36, and 29.31 μm. In particular, a prominent tail in the PDF with retrievals of $r_{eff} > 25$ μm is observed and about 5.67% of retrievals fail, mostly due to $r_{eff} > 30$ μm (i.e., $R_{2.1}$ is too low and the apparent effective radius becomes larger than the maximum value in the LUT). Conversely, a bimodal distribution for $r_{eff,o}$ is apparent and the distribution bears a resemblance to the PDF for overcast pixels. There are significantly less observations of $r_{eff,o} < 6$ μm and $r_{eff,o} > 25$ μm compared to the standard PCL results, while the 1st, 50th, and 99th percentiles of observations are 6.73, 14.60, and 26.90 μm. Overall, differences cover the range of -7.65 μm $< r_{eff} - r_{eff,o} < 12.00$ μm, which is reduced to -3.18 μm $< r_{eff} - r_{eff,o} < 6.76$ μm if only the 1st and 99th percentiles are considered. This indicates that while both overestimations and underestimations are observed for PCL pixels, clear-sky contaminations yield a primarily positive bias in retrieved effective droplet radius with a median bias of about half a micron. These findings are consistent with the reported findings in Marshak et al. (2006), where some very small and mostly very large r_{eff} can occur for PCL pixels.

Note that in this study we do not analyze the impact of three-dimensional (3-D) radiative effects (i.e., ignoring horizontal photon transport in realistic 3-D cloud structures in the 1-D radiative transfer simulations). Retrieval biases due to 3-D radiative effects are commonly associated with cloud shadows and illuminated cloud sides, among others (Barker & Liu, 1995; Chambers et al., 1997; Marshak et al., 2006). Due to increased variability in cloud top height and an abundance of cloud edges with low τ these biases can be substantial for heterogeneous, broken cumulus fields. As a result, the τ_o and $r_{eff,o}$ retrievals, while correcting for the effects of clear-sky contamination, are not necessarily the true underlying cloud properties.

3.3. Dependence on Subpixel Horizontal Resolution

The scale dependence of C_{sub}, which is illustrated in Figure 3, indicates that a decrease in subpixel horizontal resolution might induce significant uncertainties, which directly impacts the reliability of $R_{0.86,o}$ and $R_{2.1,o}$ and, subsequently, the cloud property retrieval.

A comparison of τ_o, using observations from the native horizontal resolution of 30 m, and those based on 240-m reflectances is shown in Figure 5a. A summary of the results is presented in table 2. Even though lower-resolution subpixel data were used to calculate both $\overline{R_{0.86,o}}$ and $\overline{R_{2.1,o}}$, there is overall good agreement between the two retrievals for the overcast part of PCL pixels with $r = 0.985$ and nRMSD = 8.79%. A decrease of subpixel horizontal resolution to 480 m reduces the correlation ($r = 0.941$) and increases the nRMSD to 15.55%, as shown in Figure 5b. Considering the uncertainty in C_{sub} (compared to the 30-m results) this behavior is not surprising. Distributions of the difference between τ_o from lower-resolution subpixel data and from 30-m observations is shown in Figure 5c. These PDFs can be directly compared to the distribution of $\tau - \tau_o$ in Figure 4c. Using 240-m reflectances, the 1st, 50th, and 99th percentiles of the difference are reduced to −0.94, −0.17, and 0.13, respectively (−1.66, −0.29, and 0.35 for the 480-m results). While the comparison is worse than for 240-m subpixel observations, retrieved τ_o from 480 and 30-m data still agree better than the standard retrievals from the pixel level reflectances (see Figure 4a).

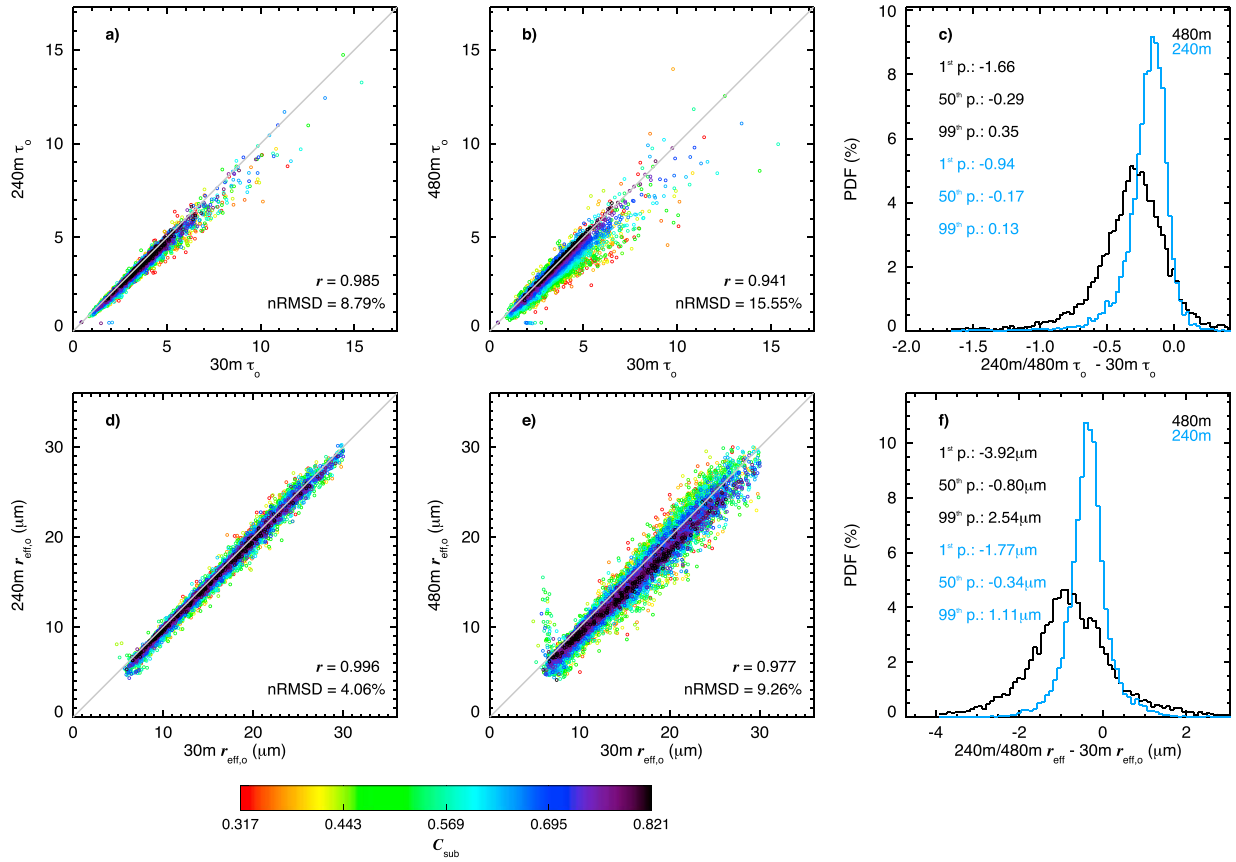

Figure 5. Comparison between retrieved cloud optical thickness based on the average 30-m reflectance of the overcast part of a partly cloudy pixel (τ_o) and τ_o based on the average (a) 240- and (b) 480-m subpixel reflectance. The pixel level scale is 960 m. Colors indicate the subpixel cloud cover (C_{sub}; from 30-m data and based on the extensive cloud masking scheme described in section 2); the gray diagonal line represents the identity line. The correlation coefficient (r) and normalized root-mean-square deviation between τ_o from 30 m and lower-resolution reflectances (nRMSD) is given. (c) Probability density functions (PDFs) of the difference between τ_o from 30-m data and 240-m (blue), as well as 480-m overcast reflectance (black), respectively. The 1st, 50th, and 99th percentiles are given. (d–f) Same as (a)–(c) but for the effective droplet radius ($r_{eff,o}$).

Retrieved $r_{eff,o}$ based on 240-m subpixel observations also agree well with the 30-m results, as shown in Figure 5d. Compared to the standard retrievals shown in Figure 4d, the correlation coefficient is increased ($r = 0.996$) and significantly reduced deviations from the identity line yield a much lower nRMSD of = 4.06%. As before, the retrieval based on 480-m data deviates more from the 30-m results, as illustrated in Figure 5e. The scatter around the identity line is increased and starts to resemble the behavior of r_{eff} shown in Figure 4e, although the correlation coefficient is still higher ($r = 0.977$) and the nRMSD is lower (9.26%). Figure 5f illustrates the PDF of the difference between $r_{eff,o}$ from the lower-resolution subpixel data and the 30-m results. Compared to the standard r_{eff} retrieval the maximum deviations are significantly reduced, as the 1st, 50th, and 99th percentiles of the difference of $r_{eff,o}$ from 240 and 30-m observations are −1.77, −0.34, and 1.11 μm, respectively (−3.92, −0.80, 2.54 μm for the 480-m results). Again, these results are summarized in Table 2.

Considering the good agreement between derived C_{sub} from 30 and 120-m data, the agreement between the respective τ_o and $r_{eff,o}$ is even better if higher-resolution subpixel data are available to calculate the average overcast subpixel reflectance following equation (1). However, at all subpixel scales the results are less biased than the standard retrieval of τ and r_{eff}, which simply utilizes the pixel level reflectances and assumes $C_{sub} = 1$.

4. Improved PCL Retrieval With Subpixel VNIR Information

The unique ASTER data set in this study provides the necessary subpixel information about C_{sub}, $R_{0.86}$ and $R_{2.1}$ at arbitrary horizontal resolutions (as long as it is > 30 m). However, most satellite-based passive sensors are characterized by more limited subpixel observations. Imagers that facilitate operational retrievals with a global coverage (e.g., MODIS and VIIRS) usually sample reflectances at much coarser spatial resolutions. The

operational MODIS C6 retrievals are performed at horizontal scales of 1,000 m and are based on aggregated VNIR and SWIR reflectances, which are observed at 250 and 500 m, respectively. Meanwhile, the VNIR and SWIR reflectances from VIIRS are sampled at a horizontal resolution of 375 m and are subsequently aggregated to 750 m for the cloud property retrieval. Other instruments (e.g., SEVIRI) only have a single high-resolution VNIR band and no high-resolution SWIR reflectances are available.

This section introduces approaches to estimate the subpixel cloud cover (section 4.1) and high-resolution $R_{2.1}$ (section 4.2) for MBL cloud scenes. These techniques make use of available subpixel VNIR reflectance observations and thus are applicable for common satellite missions. However, the analysis is geared toward a potential MODIS application and thus features similar pixel level and subpixel horizontal resolutions of 960 and 240 m. The estimated subpixel properties provide the input for a retrieval for PCL pixels following equation (1), which is evaluated in section 4.3.

4.1. Estimation of Subpixel Cloud Cover

Approaches to determine cloud cover in the presence of PCL pixels have been reported by Minnis et al. (1987), Wielicki and Parker (1992), and Coakley et al. (2005). These techniques are highly scene dependent, include observations at a thermal band to determine brightness temperatures and consist of comparisons with cloud albedo climatologies. A simpler approach is employed by the operational MODIS cloud mask product (Ackerman et al., 1998; Baum et al., 2012), which yields a binary 250-m cloudiness flag from a pair of visible reflectance thresholds. The proposed estimation of the subpixel cloud cover (C^*_{sub}; the superscript $*$ indicates the estimated value) closely follows this MODIS approach and is based on a simpler cloud masking scheme based on 240-m VNIR data. In a first step, the pixel level cloud mask value is assigned to each of the 240-m subpixels. Note that for this study the four cloudiness flags are already reduced to a binary cloud mask, as described in section 2. Subsequently, two spectral tests are performed for each subpixel of a cloudy pixel level observation. The first test is composed of a comparison of the 240-m subpixel VNIR reflectance to the 90th percentile of clear-sky pixels in the respective scene (p_{90}). The second test determines whether the color ratio of $R_{0.86}/R_{0.65}$ is within the range of two predefined thresholds (here $R_{0.65}$ indicates ASTER band 2 reflectances centered around $\lambda = 0.65\,\mu m$). This test closely resembles the third cloudiness test of the full ASTER cloud mask algorithm described in Werner et al. (2016) and is used to distinguish clouds from the darker ocean surface, as well as from measurement over land. Consequently, a subpixel is determined to be cloudy if

$$\begin{aligned} R_{0.86} &> p_{90} \quad \text{and} \\ 0.8 < \frac{R_{0.86}}{R_{0.65}} &< 1.75. \end{aligned} \tag{2}$$

It is important to emphasize the limitations of this technique, which essentially just accentuates the general uncertainties of satellite-based cloud fraction estimations. As discussed by Dey et al. (2008), Di Girolamo and Davies (1997), and Yang and Di Girolamo (2008), cloud detection algorithms should be designed individually with a particular application in mind. Its performance is affected not only by observational scale and thresholding effects but also by scene characteristics such as cloud type and surface albedo, as well as the presence of three-dimensional radiative effects and sunglint, among others. The applied cloud masking scheme in this study was designed for (and validated by) marine cumulus and stratus scenes, with only liquid phase and low to moderate aerosol turbidity, and which were sampled outside of strong sunglint and large solar zenith angles (i.e., $\theta_0 > 65°$). Consequently, the presented results in this section, which evaluate the subpixel cloud cover estimates based on equation (2), are only valid for similar cloud scenes with a high contrast in the visible spectral wavelength range between cloudy and clear pixels.

Figure 6a shows a comparison between the actually observed C_{sub} (based on 240-m data) and C^*_{sub}, derived for all cloudy 960-m pixels. Dots indicate the median of the C^*_{sub} distribution within each C_{sub} bin (in increments of 0.05), while the vertical bars illustrate the interquartile range (IQR; 75th – 25th percentile of data points). There is a high correlation between C^*_{sub} and C_{sub} with $r = 0.948$ and nRMSD= 6.40%. Most deviations from the identity line tend to be overestimations of the estimated subpixel cloud cover, which increase with decreasing C_{sub}. Since in the standard retrieval of τ and r_{eff} the PCL pixel is assumed to exhibit $C_{sub} = 1$, a slight overestimation indicates that the derived $R_{0.86,o}$ and $R_{2.1,o}$ from equation (1) fall between the actually observed values and the total reflectances at the pixel level scale. This behavior is preferable to an underestimation of C^*_{sub} (compared to the true C_{sub}), where the $R_{0.86}$ and $R_{2.1}$ would be overcorrected.

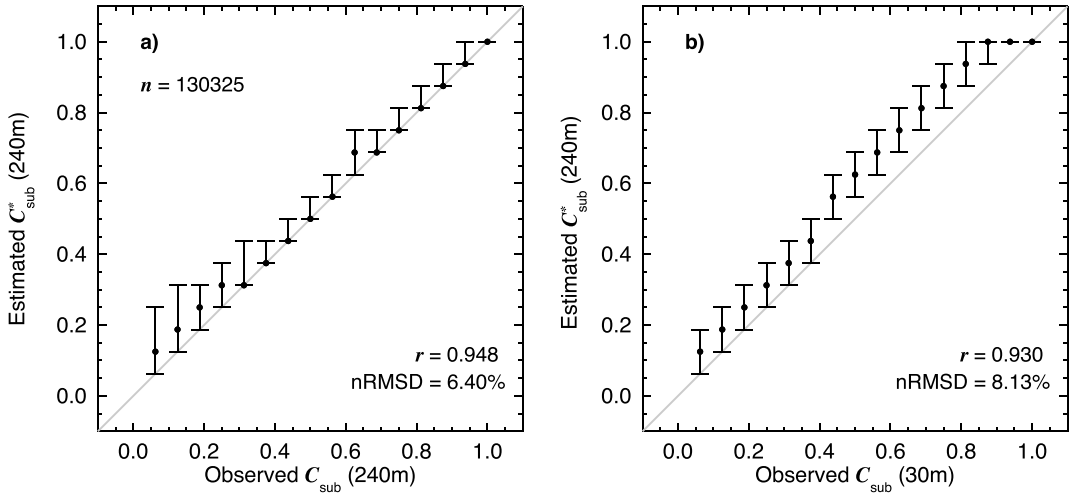

Figure 6. (a) Comparison between the actually observed subpixel cloud cover (C_{sub}; based on the extensive cloud masking scheme described in section 2) derived from 240-m data and the estimated results (C^*_{sub}; based on equation (2)). The pixel level scale is 960 m. The number of observations (n), correlation coefficient r, and normalized root-mean-square deviation between the C_{sub} and C^*_{sub} (nRMSD) is given. (b) Same as (a) but C_{sub} is derived from observations at a horizontal resolution of 30 m.

Comparing C^*_{sub} to the actually observed values from 30-m data (i.e., calculated from observations at the highest possible resolution) instead of C_{sub} at 240 m reveals that the general overestimation of C^*_{sub} becomes more prominent, as shown in Figure 6b. This is especially true for pixels with large subpixel cloud cover ($C_{sub} > 0.85$), where the estimated results almost universally exhibit $C^*_{sub} = 1$. However, for these PCL pixels the biases associated with pixel level retrievals of τ and r_{eff} are comparatively small (see Figure 3) and the impact of C^*_{sub} overestimations should be negligible. Overall, the correlation between C^*_{sub} and C_{sub} decreases ($r = 0.930$) and the bias (nRMSD = 8.13%) becomes larger when C_{sub} is derived from 30-m observations.

Considering the limitations of the approach, while keeping in mind that the comparisons are performed for marine liquid water clouds only, it can be concluded that the steps outlined in this section provide reasonable estimates of the actually observed subpixel cloud cover for the 48 MBL cloud fields in this study. Naturally, this also indicates that the binary 250-m cloudiness flag provided by MODIS yields good estimates of C^*_{sub}, at least for MBL cloud scenes in the absence of cirrus, low Sun or sunglint.

4.2. Estimation of High-resolution SWIR Observations

While many sensors provide information about the distribution of subpixel VNIR reflectances within the remotely sensed pixels, some sensors, like MODIS, even provide subpixel SWIR reflectance data, albeit at lower spatial scales. In the following paragraphs three methods are discussed, which provide estimations of $R_{2.1}$ for each subpixel, based on different assumptions and the information about the observed subpixel behavior of $R_{0.86}$.

The first method, which is referred to hereafter as *Oversampled SWIR Reflectance Approach* and is illustrated in Figure 7a, assumes that while there is variability in $R_{0.86}$ within a pixel, $R_{2.1}$ remains constant on the subpixel scale. This means that the pixel level $R_{2.1}$ value is simply assigned to each of the available subpixels, which makes this approach easy to implement and computationally inexpensive. The red triangle in the example LUT indicates a pixel with average observations of $R_{0.86} = 0.305$ and $R_{2.1} = 0.200$, while the black dots represent the position of four subpixels with varying VNIR reflectance (gray lines indicate the values $R_{0.86,i}$ and $R_{2.1,i}$ of the $i = 1 - 4$ subpixels). Since it is assumed that there is no variability in $R_{2.1,i}$ within the pixel, it follows that $R_{2.1,i} = R_{2.1} = 0.200$. To test the quality of this assumption, the inhomogeneity index $H_{\sigma,2.1}$ is calculated, which is defined as the ratio of standard deviation ($\sigma_{2.1}$) to spatial average (i.e., the pixel level value $R_{2.1}$) of subpixel SWIR reflectances (Cho et al., 2015; Di Girolamo et al., 2010; Liang et al., 2009; Zhang & Platnick, 2011; Zhang et al., 2012):

$$H_{\sigma,2.1} = \frac{\sigma_{2.1}}{R_{2.1}}. \quad (3)$$

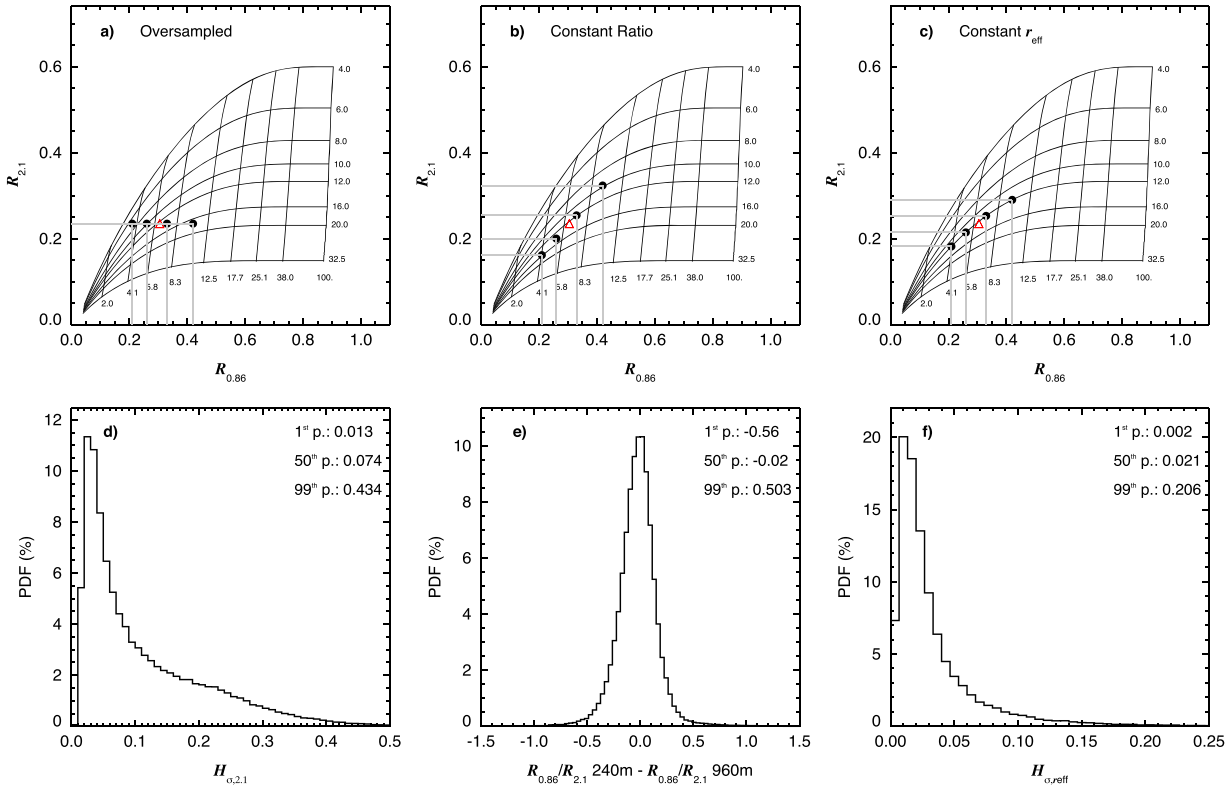

Figure 7. (a) Example lookup table to illustrate the *Oversampled SWIR Reflectance Approach*. The red triangle indicates the mean $R_{0.86}$ and $R_{2.1}$ of a pixel, while the black dots illustrate $R_{0.86}$ of four subpixels and the respective $R_{2.1}$ based on the Oversampled SWIR Reflectance approach. Gray vertical and horizontal lines are visual aids. (b and c) Same as (a) but illustrating the *Constant Reflectance Ratio Approach* and *Constant r_{eff} Approach*, respectively. (d) Probability density function of the subpixel variability of $R_{2.1}$ ($H_{\sigma,2.1}$). The subpixel and pixel level scale is 240 and 960 m, respectively. (e) Same as (d) but for the difference of the ratio of $R_{0.86}$ to $R_{2.1}$. (f) Same as (d) but for the subpixel variability of the effective droplet radius (H_{σ,r_eff}).

Figure 7d shows the PDF of observed $H_{\sigma,2.1}$ for all cloudy ASTER pixels. The pixel level and subpixel scale is 960 and 240 m, respectively. The peak of the distribution is found around low values of $H_{\sigma,2.1} \approx 0.03$, which is representative of rather homogeneous distributions. However, there are a multitude of pixels with significantly higher values that are associated with inhomogeneous pixels. The 1st, 50th, and 99th percentiles of $H_{\sigma,2.1}$ observations is 0.013, 0.074, and 0.434. This indicates that for the sampled cloud fields in this study there is a nonnegligible subpixel variability in $R_{2.1}$ and that a general assumption of $H_{\sigma,2.1} = 0$ is not appropriate.

A second approach is based on the assumption that the inhomogeneity index of the VNIR reflectance equals $H_{\sigma,2.1}$ (i.e., spectrally consistent subpixel deviations from the spatially averaged reflectance):

$$\begin{aligned} H_{\sigma,2.1} &= H_{\sigma,0.86} \\ \frac{\sigma_{2.1}}{R_{2.1}} &= \frac{\sigma_{0.86}}{R_{0.86}} \\ \frac{\sqrt{\frac{1}{n-1}\cdot\sum_{i=1}^{i=n}(R_{2.1,i}-R_{2.1})^2}}{R_{2.1}} &= \frac{\sqrt{\frac{1}{n-1}\cdot\sum_{i=1}^{i=n}(R_{0.86,i}-R_{0.86})^2}}{R_{0.86}}, \end{aligned} \tag{4}$$

where the index $i = 1, 2, \ldots, n$ indicates each of the n available subpixels. Additionally, if deviations of individual subpixel reflectances from the average (pixel level) values are similar for both bands (i.e., $R_{2.1,i} - R_{2.1} = R_{0.86,i} - R_{0.86}$), equation (4) can be simplified to

$$\frac{R_{2.1,i}}{R_{0.86,i}} = \frac{R_{2.1}}{R_{0.86}}. \tag{5}$$

Equation (5) suggests that the ratio of SWIR to VNIR reflectance at the subpixel scale is equal to the ratio of the pixel level results. Consequently, this method is called *Constant Reflectance Ratio Approach* and is illustrated

in Figure 7b. Similar to Figure 7a, the pixel level reflectances of $R_{0.86} = 0.305$ and $R_{2.1} = 0.235$ are indicated by a red triangle in the example LUT. While the individual subpixels have the same $R_{0.86,i}$ as before, the corresponding estimates of $R_{2.1,i}$ show some variability. Positive and negative $R_{0.86,i}$ deviations from the pixel level VNIR reflectance yield positive and negative $R_{2.1,i}$ deviations from $R_{2.1}$, respectively. To test the viability of the assumption in equation (5), the PDF of the difference between subpixel and pixel level SWIR to VNIR reflectance ratio (i.e., $\frac{R_{2.1,i}}{R_{0.86,i}} - \frac{R_{2.1}}{R_{0.86}}$) is calculated and shown in Figure 7e. These ratios are derived for all cloudy 960-m ASTER pixels, while the subpixel horizontal resolution is 240 m. The 1st, 50th, and 99th percentiles of the calculated differences are −0.56, −0.02, and 0.50. However, 50% of observations are in the range −0.13–0.07 (i.e., a difference between subpixel and pixel level reflectance ratio of $\leq$ 13%) and the median is close to 0. This indicates that for a majority of observations the assumption of constant reflectance ratios at different scales is reasonable.

A third approach to estimate $R_{2.1,i}$ assumes a constant r_{eff} within a pixel. Since the relationship between retrieved cloud properties and cloud top reflectance is determined by the LUT, each $R_{2.1,i}$ can be derived via interpolation of the modeled SWIR reflectances at the position of each $R_{0.86,i}$ along the respective r_{eff} isoline. This *Constant r_{eff} Approach* is illustrated in Figure 7c, where individual $R_{2.1,i}$ align with the $r_{eff} = 12$ µm-isoline. The appropriate r_{eff} isoline can be determined in different ways: (i) depending on the retrieved pixel level cloud properties the interpolation is performed along the isoline corresponding to the closest r_{eff} that exists in the LUT simulations. Depending on the r_{eff} resolution of the applied LUT (i.e., the r_{eff} values for which simulations exist) this can lead to substantial uncertainties, while the computational costs are low. (ii) Interpolated LUT values are generated for the retrieved τ and r_{eff}, which reduces uncertainty and increases computational costs. To test whether the assumption of constant r_{eff} within a pixel is reasonable, the inhomogeneity index with regard to the effective radius ($H_{\sigma,r_{eff}}$; defined as the ratio of standard deviation to spatial average of subpixel r_{eff} at 240 m) is calculated for all cloudy pixels with a horizontal resolution of 960 m. Figure 7f shows the PDF of $H_{\sigma,r_{eff}}$, which is visibly narrower than the PDF of $H_{\sigma,2.1}$ in Figure 7d. The 1st, 50th, and 99th percentiles of observations are 0.00, 0.02, and 0.21, which suggests that a majority of ASTER pixels indeed exhibit little variability in subpixel r_{eff}.

Each of the proposed approaches offers advantages and disadvantages. The Oversampled SWIR Reflectance Approach is simple and computationally inexpensive, but based on the PDF of observed $H_{\sigma,2.1}$ in Figure 7d this method might result in significant uncertainties in the estimation of $R_{2.1,i}$. Meanwhile, ASTER observations indicate that the assumptions in the Constant Reflectance Ratio Approach seem reasonable. While this method is computationally inexpensive, it is only valid for thinner clouds, where τ and r_{eff} are strongly correlated (note the almost linear increase of the r_{eff} isolines in Figure 7 for $\tau < 8$). Conversely, for $\tau > 17$ the $R_{0.86}$ sensitivity to τ is nearly orthogonal to the $R_{2.1}$ sensitivity to r_{eff} (i.e., the respective isolines become orthogonal). As a result, large subpixel $R_{0.86}$ variability is associated with low $R_{2.1}$ variability for such pixels. Finally, the *Constant r_{eff} Approach* requires a successful cloud property retrieval, which has been shown to frequently fail for pixels with very low C_{sub}. Moreover, the pixel level r_{eff} can be significantly biased due to clear-sky contamination (see biases in Figure 4), as well as the plane-parallel homogeneous bias (Marshak et al., 2006; Werner et al., 2018; Zhang et al., 2016), which describes the difference between pixel level retrievals and the spatial average of the subpixel results. For such observations the derivation of $R_{2.1,i}$ is performed along a wrong isoline. Note that if applied to MODIS observations, 250-m SWIR reflectances can be estimated from actually observed $R_{2.1}$ at 500 m, while the retrieval products are provided at horizontal resolutions of 1,000 m. Thus, applying this approach for such geometries requires an additional 500-m retrieval of r_{eff}, which would increase the computational costs even further.

To evaluate the three techniques with ASTER data, joint PDFs of actually observed $R_{2.1}$ at a horizontal resolution of 240 m and the estimated results ($R^*_{2.1}$; the superscript $*$ again indicates the estimated value) are calculated and shown in Figure 8 for (a) the Oversampled SWIR Reflectance Approach, (b) the Constant Reflectance Ratio Approach, and (c) the Constant r_{eff} Approach. The first two approaches are facilitated by pixel level $R_{2.1}$, which were sampled above all cloudy 960-m pixels. To minimize the influence of clear-sky contamination and the plane-parallel homogeneous bias, the respective r_{eff} isoline in the Constant r_{eff} Approach is determined from the spatial average of actually observed 240-m retrievals and not from the pixel level result.

The Oversampled SWIR Reflectance Approach yields the lowest correlation ($r = 0.980$) and largest bias (nRMSD = 9.36%) between $R_{2.1}$ and $R^*_{2.1}$, although the majority of observations are concentrated around the identity line. The comparison improves noticeably for the Constant Reflectance Ratio Approach, where

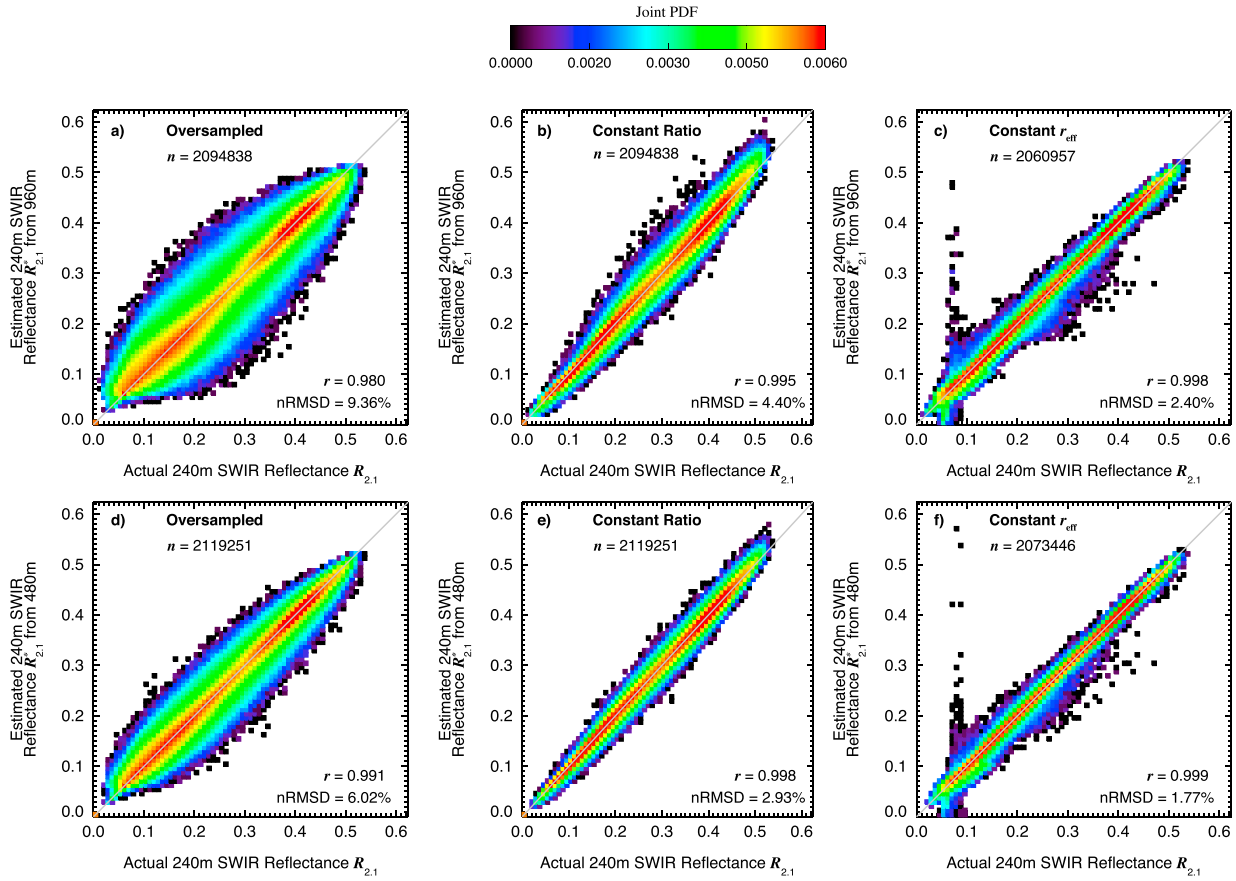

Figure 8. (a) Joint probability density function of actually observed 240-m shortwave-infrared (SWIR) reflectance ($R_{2.1}$) and estimated $R_{2.1}$ based on the *Oversampled SWIR Reflectance Approach*. The estimation is facilitated by observed $R_{2.1}$ at a horizontal resolution of 960 m. Only cloudy 960-m pixels are considered in the analysis. The number of observations (n), correlation coefficient r, and normalized root-mean-square deviation between observed and estimated $R_{2.1}$ (nRMSD) are given. (b and c) Same as (a) but the estimation is based on the *Constant Reflectance Ratio Approach* and *Constant* r_{eff} *Approach*, respectively. (d–f) Same as (a–c) but the estimation is based on observed $R_{2.1}$ at a horizontal resolution of 480 m.

$r = 0.995$ and the bias is reduced to nRMSD = 4.40% (i.e., less than half the bias of the first method). Both approaches yield $n = 2,094,838$ high-resolution $R^*_{2.1}$ values. However, due to the extra constraint of a successful effective radius retrieval, this number is reduced by about 34,000 data points (2%) if the Constant r_{eff} Approach is applied. While this method results in the highest correlation (0.998) and lowest bias (nRMSD = 2.40%; almost half the bias of the Constant Reflectance Ratio Approach, some significant overestimation and underestimations of $R^*_{2.1}$ are observed. This is not surprising, because the approach assumes a successful cloud property retrieval along a fixed r_{eff} isoline. If some of the subpixels deviate substantially from this line, or are positioned outside the LUT, the error in $R^*_{2.1}$ can become quite large. If the pixel level horizontal resolution is increased to 480 m (i.e., closely resembling the MODIS geometry), the comparisons improve noticeably. Correlation coefficients increase to $r = 0.991, 0.998, 0.999$ for the three approaches, while the biases are reduced to nRMSD = 6.02%, 2.93%, and 1.77%. The number of successful $R^*_{2.1}$ estimations is slightly increased, which can be explained by the increase in the number of cloudy pixels at 480 m. As before, this number is lower for the *Constant* r_{eff} *Approach*, where a successful cloud property retrieval is required.

Both the Constant Reflectance Ratio Approach and Constant r_{eff} Approach yield reasonable estimates of $R^*_{2.1}$. However, depending on the magnitude of the bias in the pixel level r_{eff} retrieval, employing the Constant r_{eff} Approach for a PCL observation requires multiple retrieval iterations. During each iteration the new estimate of $r_{\text{eff,o}}$ provides a more reliable isoline for the $R^*_{2.1}$ interpolation. This makes the Constant r_{eff} Approach computationally less efficient in comparison to the other two approaches. Note that due to the better comparison with actual ASTER observations for small $R_{2.1,i}$ (which are more common in PCL pixels) the cloud property retrievals in the following sections have been derived with the Constant Reflectance Ratio Approach.

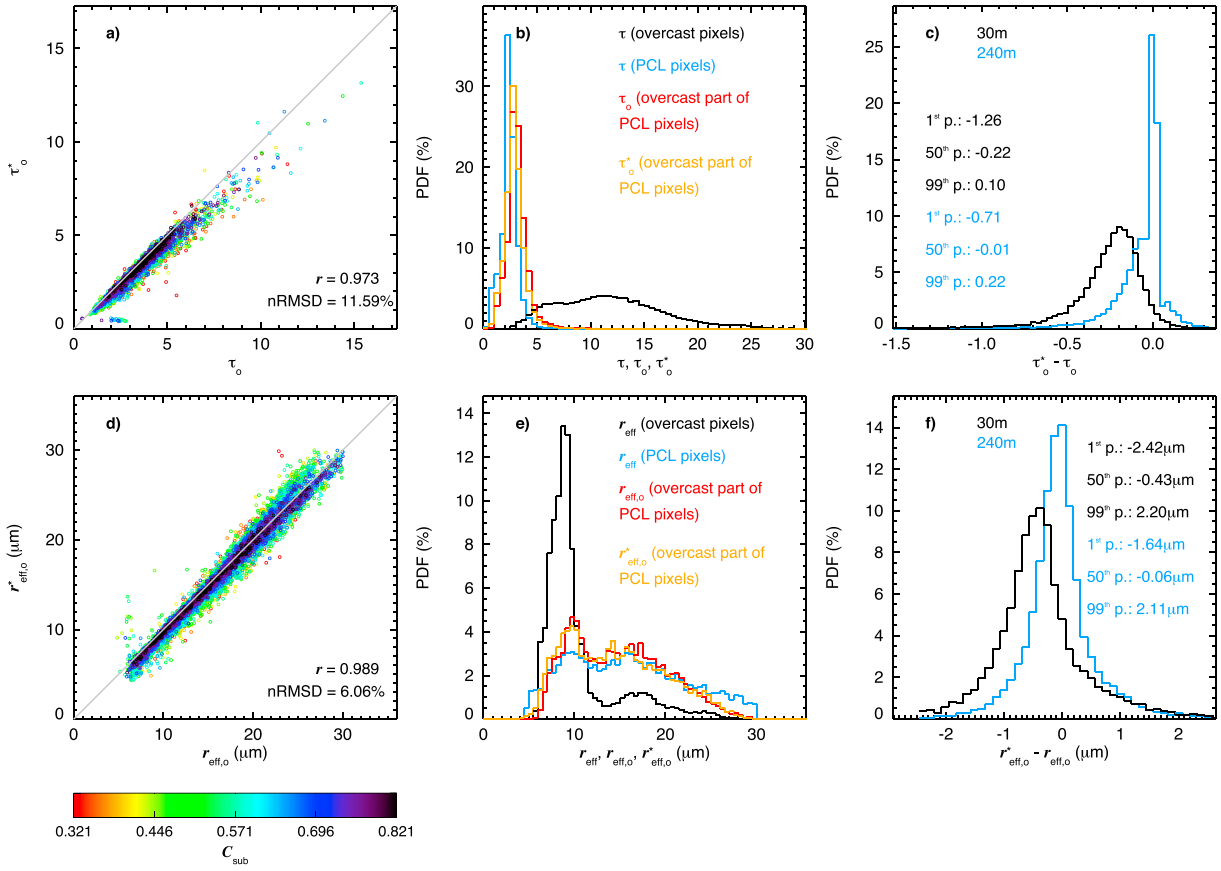

Figure 9. (a) Comparison between retrieved cloud optical thickness based on the average 30-m reflectance of the overcast part of a pixel (τ_o) and the cloud optical thickness based on estimations for C^*_{sub} and $R^*_{2.1}$ from the *Constant Reflectance Ratio Approach* (τ^*_o). Colors indicate the subpixel cloud cover (C_{sub}; based on the extensive cloud masking scheme described in section 2); the gray diagonal line indicates the identity line. The correlation coefficient r and normalized root-mean-square deviation between τ_o and τ^*_o (nRMSD) is given. (b) Same as Figure 4b but also including a probability density function (PDF) of τ^*_o (orange). (c) PDF of the difference between τ^*_o and τ_o for all PCL pixels (black), as well as between τ^*_o and τ_o based on the average 240 m reflectance of the overcast part of a pixel (blue). The respective 1st, 50th, and 99th percentiles are given. (d–f) Same as (a–c) but for the effective droplet radius $r_{eff,o}$, $r^*_{eff,o}$, and r_{eff}.

4.3. Evaluation of Estimated PCL Retrieval

Section 4.1 demonstrates that information about the subpixel VNIR distribution can be used to infer reasonable estimates of the subpixel cloud cover, while section 4.2 introduces methods to reliably estimate the SWIR reflectance for each subpixel. Both provide the means to calculate the average of estimated cloudy reflectances, that is, $\overline{R^*_{0.86,o}}$ and $\overline{R^*_{2.1,o}}$ in equation (1), and subsequently retrieve τ^*_o and $r^*_{eff,o}$ (as before, the superscript $*$ indicates the estimated value). Naturally, any uncertainty in the respective estimations will induce an uncertainty in the derived cloud properties.

Figures 9a and 9d show a comparison between τ^*_o and $r^*_{eff,o}$ and the respective τ_o and $r_{eff,o}$, which are based on ASTER observations at 30-m horizontal resolution. The estimated retrievals are based on the Constant Reflectance Ratio Approach with $R_{2.1}$ samples at 480 m; as before the analysis is performed for all cloudy PCL pixels with a horizontal resolution of 960 m. This geometry allows not only for a direct comparison to the results in Figure 4 but also for an evaluation of the estimated retrieval for PCL pixels (based on equation (1)) in regard to a potential MODIS application. Derived τ^*_o agree well to the actually observed τ_o with $r = 0.973$ and a reduced bias of nRMSD = 11.59%, which resembles a significant improvement from the standard retrieval based on the pixel level reflectance. A similarly improved comparison between $r_{eff,o}$ and $r^*_{eff,o}$ is shown in Figure 9d, where the correlation is increased ($r = 0.989$) and the bias is reduced (from nRMSD = 13.74% to nRMSD = 6.06%). As a result, the PDFs of τ^*_o and $r^*_{eff,o}$ (orange) in Figures 9b and 9e closely resemble the respective distributions of τ_o and $r_{eff,o}$. The improvement from the standard retrieval is particularly obvious for the effective droplet radius, where the prominent tail of large $r_{eff} > 25$ μm is not observed for $r^*_{eff,o}$. Similar to Figures 4c and 4f, PDFs of the remaining biases between estimated and observed cloudy part retrievals (black

Table 3
The 1st, 50th, and 99th Percentiles of the Difference $\tau_o^* - \tau_o$ and $r_{eff,o}^* - r_{eff,o}$

	$\tau_o^* - \tau_o$			$r_{eff,o}^* - r_{eff,o}$		
Approach	1st	50th	99th	1st	50th	99th
Standard	−3.74	−0.47	−0.07	−3.27 μm	0.84 μm	6.16 μm
Oversampled SWIR Reflectance	−0.66	0.01	0.30	−0.38 μm	1.67 μm	9.00 μm
Constant Reflectance Ratio	−0.71	−0.01	0.22	−1.64 μm	−0.06 μm	2.11 μm
Constant r_{eff}	−0.53	0.00	0.25	−0.90 μm	0.43 μm	3.20 μm

Note. Statistics are given for the *Oversampled SWIR Reflectance*, *Constant Reflectance Ratio*, and *Constant r_{eff} Approaches*. Also, the statistics for the difference between standard partly cloudy retrievals, which are based on the average pixel level reflectance, and τ_o and $r_{eff,o}$ are also presented. The pixel level and subpixel horizontal resolutions are 960 and 240 m, respectively. SWIR = shortwave-infrared.

lines) are shown in Figures 9c and 9e. The distributions are much narrower, as the 1st, 50th, and 99th percentiles of the difference $\tau_o^* - \tau_o$ are −1.26, −0.22, and 0.10 (2.42, −0.43, 2.20 μm for the difference $r_{eff,o}^* - r_{eff,o}$). These statistics are also very similar to the 240-m results from the scale analysis in Figures 5c and 5f. If τ_o^* and $r_{eff,o}^*$ are compared to τ_o and $r_{eff,o}$ from 240-m subpixel observations (instead of the high-resolution 30-m results), the differences become even smaller (blue lines). Here the 1st, 50th, and 99th percentiles of the difference $\tau_o^* - \tau_o$ are −0.71, −0.01, and 0.22 (1.64, −0.06, 2.11 μm for the difference $r_{eff,o}^* - r_{eff,o}$).

The remaining biases between τ_o^* and $r_{eff,o}^*$ from the three approaches highlighted in section 4.2 and the actually observed cloud retrievals at 240 m are summarized in Table 3. To provide the appropriate reference statistics, the differences $\tau - \tau_o$ and $r_{eff} - r_{eff,o}$ (i.e., the performance of the standard retrieval approach) are also listed. Regarding the difference $\tau_o^* - \tau_o$ the three approaches described in section 4.2 yield considerable improvements in comparison to the standard retrieval. Statistics for the three methods are very similar and highlight that the estimated retrieval for PCL pixels can effectively mitigate the bias introduced by clear-sky contamination (i.e., a median difference close to 0). Larger variability between the three approaches exist for the differences of $r_{eff,o}^* - r_{eff,o}$. Considering the uncertainties in $R_{2.1}^*$ shown in Figure 8a, the differences for the Oversampled SWIR Reflectance Approach are characterized by the largest 50th and 99th percentiles that are even larger than the ones from the standard retrieval. This approach can also not mitigate the extended tail of $r_{eff} > 25$ μm in the PDF (however, it minimizes observations of very small $r_{eff,o} < 6$ μm). Both the Constant Reflectance Ratio Approach and Constant r_{eff} Approach provide considerable improvements and the retrievals exhibit substantially reduced biases. Distributions of $r_{eff,o}^*$ have no tail of large droplets for either approach and the PDFs look almost indistinguishable. The Constant Reflectance Ratio Approach yields a minimum median difference between $r_{eff,o}$ and $r_{eff,o}^*$ (it also has the lowest 99th percentile). Note that while the respective deviations become larger, these conclusions do not change when τ_o and $r_{eff,o}$ are derived from 30-m data.

The results in Figure 9 and Table 3 illustrate that for the 48 MBL cloud scenes in this study the estimations presented in sections 4.1 and 4.2 yield retrievals, which correspond to the cloudy part of PCL pixels and agree well with the actually observed ASTER properties. This approach is directly applicable to MODIS observations and represents a significant improvement over the standard retrieval, which simply utilizes the pixel level observations of $R_{0.86}$ and $R_{2.1}$.

5. Impact on Liquid Water Path and Droplet Number Concentration

Retrievals of τ and r_{eff} are widely used to infer the *LWP* and the cloud droplet number concentration (N). Both parameters are key variables for studies of aerosol-cloud interactions (Albrecht, 1989; Twomey, 1974) and the subsequent radiative forcing (Lohmann et al., 2010; Ramaswamy & Chen, 1993). Therefore, it is essential to evaluate how these parameters are biased, when they are derived for PCL pixels.

The *LWP* can be calculated from the product of τ and r_{eff} (Brenguier et al., 2000; Miller et al., 2016):

$$LWP = \Gamma \cdot \rho_l \cdot \tau \cdot r_{eff}, \tag{6}$$

where ρ_l and Γ are the density of liquid water and a coefficient, which accounts for the vertical cloud profile. For vertically homogeneous clouds $\Gamma = 2/3$. Relating the retrieved cloud variables to N requires a number of

assumptions and simplifications (Bennartz, 2007; Brenguier et al., 2000; Schüller et al., 2005):

$$N = \alpha \cdot \tau^{0.5} \cdot r_{\text{eff}}^{-2.5}, \tag{7}$$

with $\alpha = 1.37 \cdot 10^{-5}$ following Quaas et al. (2006). As before, for PCL pixels both parameters can be derived from (i) τ and r_{eff}, which represent the biased results due to clear-sky contamination; (ii) τ_o and $r_{\text{eff,o}}$, which correspond to the parameters from the overcast part of a pixel; and (iii) τ_o^* and $r_{\text{eff,o}}^*$, which are the estimated results that mitigate the PCL bias. The analysis in section 3.2 reveals an overall negative and positive bias in retrieved τ and r_{eff}, respectively. This would indicate an overall negative bias for derived N, while the bias in LWP could be either positive or negative, depending on whether the τ or r_{eff} contribution dominates.

Figure 10a shows a comparison between derived LWP_o, which is based on τ_o and $r_{\text{eff,o}}$ at a horizontal resolution of 30 m, and the standard results of LWP for all PCL pixels. The relationship looks similar to the one for τ, which is illustrated in Figure 4a, as there are strong underestimations of LWP with $r = 0.937$ and nRMSD = 27.48%. The 1st, 50th, and 99th percentiles of the normalized difference between LWP and LWP_o (defined as the difference between both parameters, divided by LWP_o) are −72%, 18.67%, and 1.40% (corresponding to absolute differences of −35.1, −5.1, and 0.46g/m^2). The respective distribution is almost exclusively comprised of negative values, as shown in Figure 10b. These biases are drastically reduced, if the liquid water path is derived from τ_o^* and $r_{\text{eff,o}}^*$. Figure 10c shows the normalized difference between LWP_o^* and LWP_o. Similar to previous Figures, LWP_o^* is derived from 240-m subpixel reflectances and compared to LWP_o based on both 30 (black) and 240-m (blue) subpixel data. Naturally, the estimated results compare best to LWP_o at 240 m, where the 1st, 50th, and 99th percentiles of the normalized difference are −26.21%, −1.72%, and 10.70%. However, even compared to the 30-m results of LWP_o there is a significant improvement, if the derivation is based on τ_o^* and $r_{\text{eff,o}}^*$ instead of the standard results.

Figures 10d–10f illustrate the relationships between N, N_o, and N_o^*, which are derived from τ and r_{eff}, τ_o, and $r_{\text{eff,o}}$, as well as τ_o^* and $r_{\text{eff,o}}^*$, respectively. The pixel level comparison between N_o and N reveals a lot of scatter, a lower correlation ($r = 0.871$) and a rather large bias (nRMSD = 51.66%). Besides the expected underestimation in N a number of samples with large overestimations are apparent, which are associated with small effective radius retrievals around 5 μm. While these observations, which exhibit a relative difference in droplet number concentration of >40%, exist for only 3.6% of all PCL pixels, they still have a sizable statistical impact. The 1st, 50th, and 99th percentiles of the relative difference are −68.37%, −18.41% and 104.15% (i.e., absolute differences of −42.7, −4.3, and 101.2 cm^{-3}). The median biases, as well as the minimum and maximum deviations, are reduced significantly when N_o^* is compared to N_o. The median of normalized differences between the two variables at 240 m is 0.77%, while the 1st and 99th percentiles are −25% and 31.81%, respectively.

The analysis in this section shows that there are significant biases in LWP and N, if both are derived for PCL pixels. A derivation based on equation (1) and the approaches detailed in sections 4.1 and 4.2 not only mitigates the overall biases for the analyzed cloud scenes but also drastically reduces the range of observed deviations from the actually observed cloud properties.

6. Validation With Extensive ASTER Data Set

The previous analysis in this study is based on the ASTER data set described in Werner et al. (2016) and Werner et al. (2018), which consists of 48 marine altocumulus and broken cumulus scenes sampled off the coast of California. While there are a number of granules with scene cloud covers <25%, most scenes are characterized by a cloud fraction of >75%. Observations from these cloud fields were carefully colocated with the simultaneous MODIS samples and comparisons of retrieved cloud properties exhibit a good agreement with the operational MODIS C6 products (Werner et al., 2016). In this section we applied the proposed PCL retrieval approach to 446 ASTER scenes sampled over the tropical western Atlantic Ocean (12–20°N, 55–66°W) between September and December 2004 during the RICO campaign (Rauber et al., 2007), over the Gulf of Mexico (26–30°N, 90–98°W) between July and September 2006 during the GoMACCS campaign, and over the Indian ocean (5°S to 12°N, 68–78°E) between November 2006 and April 2007. More information about these scenes is given in Zhao et al. (2009).

These broken cumulus fields are characterized by small cloud sizes, generally low scene cloud fractions (with a median scene cloud cover of 7.79%) and the occasional presence of land surfaces (due to the inclusion of small islands), while a handful of scenes even exhibit noticeable sunglint. Furthermore, these scenes have not

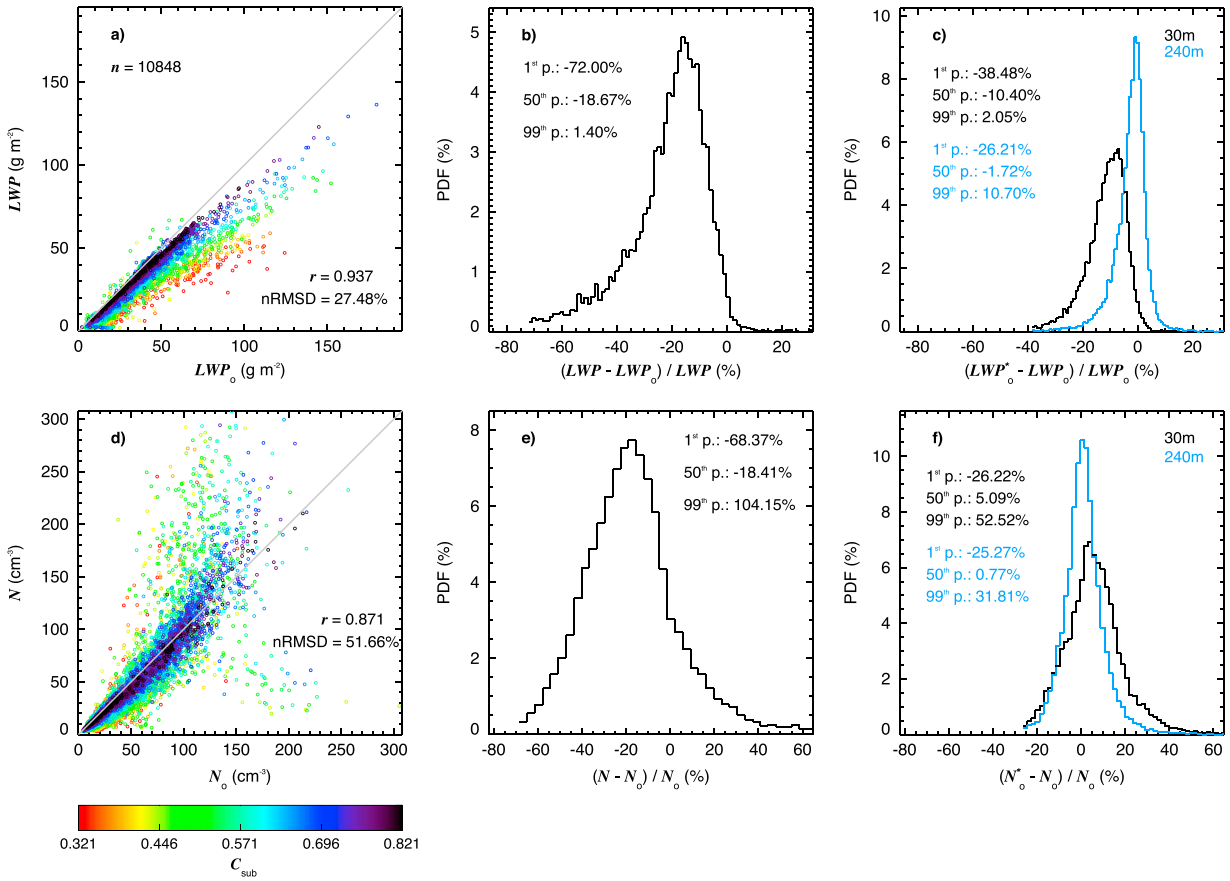

Figure 10. (a) Comparison between derived liquid water path (*LWP*) based on the average 30-m reflectance of the overcast part of a pixel (LWP_o) and the one derived from the total reflectance. Colors indicate the subpixel cloud cover (C_{sub}; based on the extensive cloud masking scheme described in section 2); the gray diagonal line indicates the identity line. The number of observations (*n*), correlation coefficient *r*, and normalized root-mean-square deviation between LWP_o and *LWP* (nRMSD) is given. (b) Probability density function (PDF) of the difference between *LWP* and LWP_o, normalized by LWP_o, for all PCL pixels. The 1st, 50th, and 99th percentiles are given. (c) PDF of the difference between derived liquid water path based on $R^*_{2.1,o}$ at 30 m (black), as well as 240 m (blue), from the *Constant Reflectance Ratio Approach* (LWP^*_o) and LWP_o, normalized by LWP_o, for all PCL pixels. (d–f) Same as (a)–(c) but for the cloud droplet number concentrations *N*, N_o and N^*_o.

been colocated with the respective MODIS observations and, as a result, the retrieved cloud properties have not been compared to the operational MODIS C6 results. However, this comprehensive data set provides the opportunity to test the viability of the assumptions and estimations in sections 4.1 and 4.2 under more complex observational conditions. While the correlation between C^*_{sub} and C_{sub} (based on 240-m data) for these scenes is $r = 0.781$, the bias is significantly larger with nRMSD = 35.46%. Most of the deviations occur for $C_{sub} < 0.2$, where a pixel level cloud property retrieval fails in more than 54% of cases (because reflectances are too small and fall outside the LUT) and the median of successful $\tau = 1.12$. Here, the average overestimation of C^*_{sub} is 32.97%. For pixels with $C_{sub} > 0.2$ there is an average overestimation of C^*_{sub} of 7.62% and $r = 0.834$. Similarly, there are slightly lower correlation coefficients and increased biases between $R^*_{2.1}$ and $R_{2.1}$ (at 240-m horizontal resolution) of $r = 0.991$ and nRMSD = 8.16%, if determined from the Constant Reflectance Ratio Approach.

Figure 11 illustrates how the increased uncertainties in C^*_{sub} and $R^*_{2.1}$ impact the cloud property retrieval for PCL pixels. PDFs of τ (i.e., the standard retrieval approach; black), τ_o (i.e., the retrieval based on the observed $\overline{R_{0.86,o}}$ and $\overline{R_{2.1,o}}$; blue) and τ^*_o (i.e., the retrieval based on the estimated $\overline{R^*_{0.86,o}}$ and $\overline{R^*_{2.1,o}}$; red) are shown in Figure 11a. The distributions are based on $n = 54,328$ cloudy PCL pixels at a horizontal resolution 960 m, while τ^*_o is derived from the Constant Reflectance Ratio Approach. The subpixel horizontal resolution is 240 m. While the distribution of τ^*_o is slightly shifted toward smaller values, it can reliably reproduce the shape and range of the τ_o distribution. The 1st, 50th, and 99th percentiles of the normalized difference between τ and τ_o are −79.89%, −37.86%, and 1.37%. In contrast, the comparison between τ^*_o and τ_o becomes significantly better

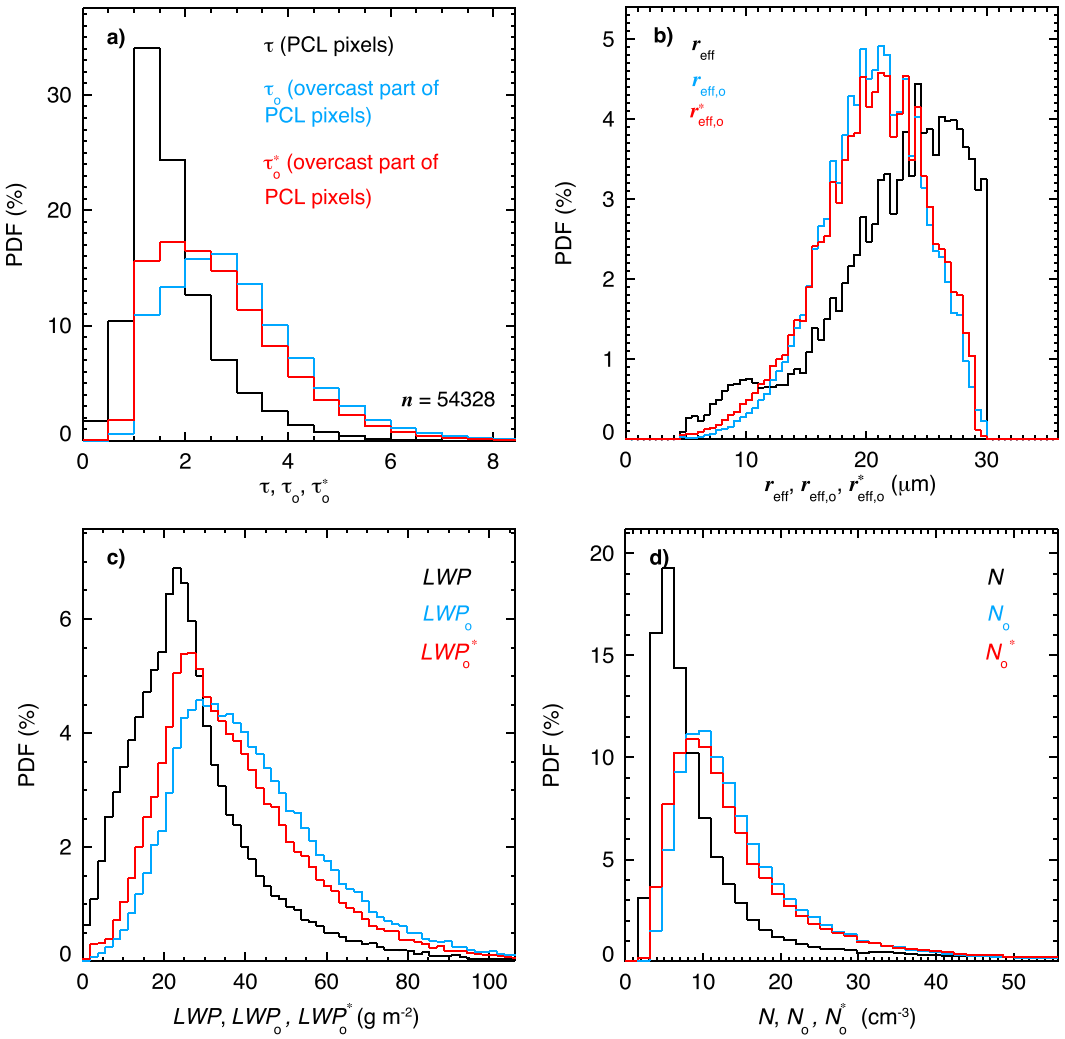

Figure 11. (a) Probability density function (PDFs) of the cloud optical thickness derived from the standard retrieval approach (τ; black), only from cloudy subpixel reflectances based on equation (1) (τ_o; blue), and the estimated overcast reflectances based on the assumptions detailed in sections 4.1 and 4.2 (τ_o^*; red). Data are from cloudy PCL pixels, which were observed over marine broken cumulus scenes (Zhao et al., 2009). The pixel level and subpixel horizontal resolutions are 960 and 240 m, respectively. (b–d) Same as (a) but for the effective droplet radius (r_{eff}, $r_{eff,o}$, and $r^*_{eff,o}$), liquid water path (LWP, LWP_o, and LWP^*_o), and cloud droplet number concentration (N, N_o and N^*_o), respectively.

with percentiles of −52.75%, −6.01%, and 9.07%, respectively. Similar improvements are observed for the effective droplet radius, liquid water path, and droplet number concentration, illustrated in Figures 11b–11d. The 1st, 50th, and 99th percentiles of the normalized difference between r_{eff} and $r_{eff,o}$ are −48.96%, 6.80%, and 62.13%, which improves to −25.33%, −0.16%, and 24.63% for $r^*_{eff,o}$. Most importantly, about 36.81% of all pixel level retrievals with the standard approach fail, predominantly because $R_{2.1}$ becomes too low (i.e., the retrieved r_{eff} would be larger than the maximum value in the LUT). This finding is similar to the one in Cho et al. (2015), who reported that for marine liquid water clouds about 33.81% of MODIS 2.1 μm retrievals fail. Conversely, observations with very large values are almost non-existent for $r_{eff,o}$ and $r^*_{eff,o}$. Meanwhile, differences between LWP and LWP_o exhibit percentiles of −88.14%, −33.76%, and 4.37%, while those between N and N_o are −84.26%, −32.61%, and 216.83% (as for the California scenes, there is a general underestimation in N for PCL pixels, but maximum deviations can be very large). Comparing the observed results for the cloudy part of PCL pixels to LWP^*_o and N^*_o yields much better agreements and the respective percentiles become −58.88%, −7.72%, and 10.59% (LWP^*_o) and −58.31%, −1.59%, and 91.97% (N^*_o).

The complex nature of these scenes seems to have no discernible negative impact on the reliability of the retrieval of the estimated cloud products τ^*_o, $r^*_{eff,o}$, LWP^*_o, and N^*_o and the significant improvements observed

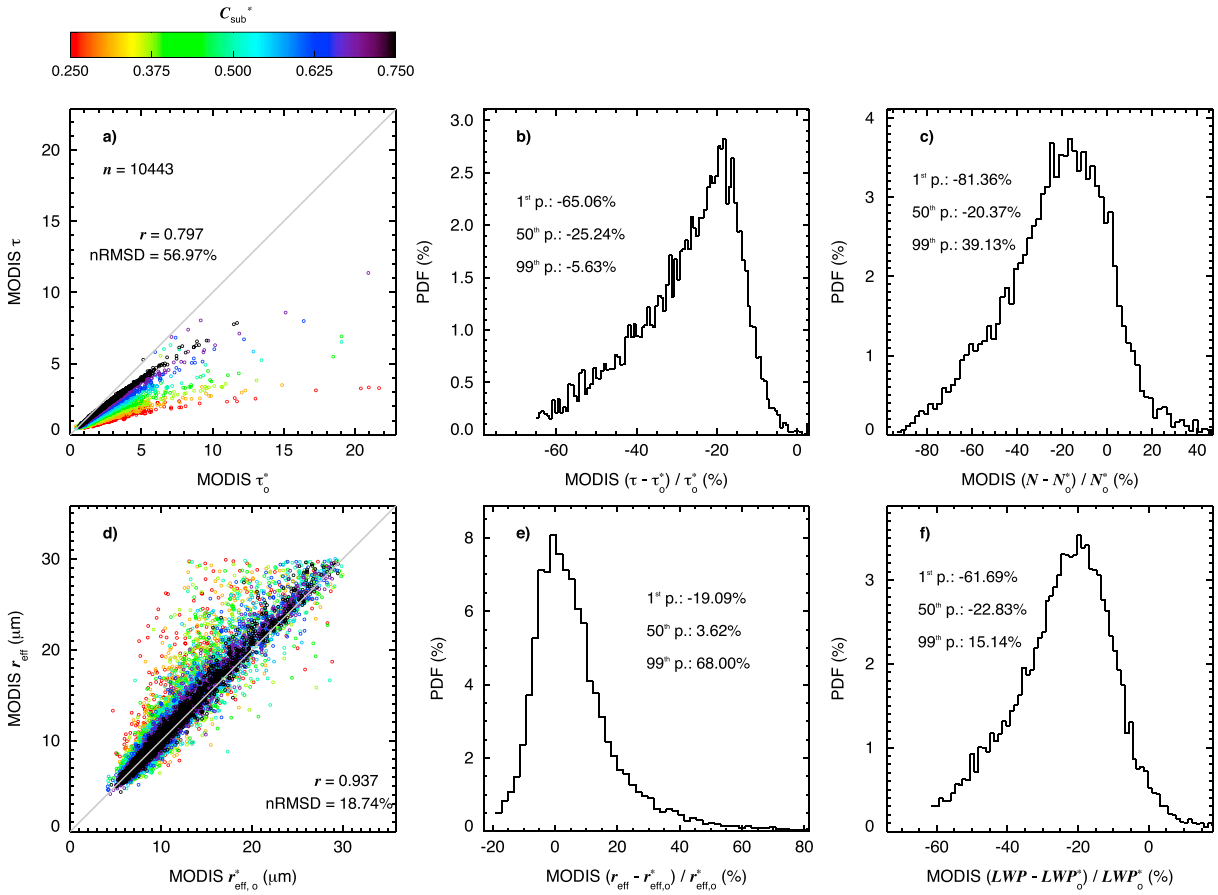

Figure 12. (a) Comparison between retrieved cloud optical thickness based on estimations for C_{sub}^* and $R_{2.1}^*$ from the *Constant Reflectance Ratio Approach* (τ_o^*) and the one retrieved from aggregated reflectance (τ). Data are from all (estimated) MODIS partly cloudy pixels, which were observed over the 48 marine altocumulus and broken cumulus scenes over the Pacific Ocean off the Coast of California (see section 2). Colors indicate the estimated subpixel cloud cover (C_{sub}^*; based on equation (2) and 250-m Moderate Resolution Imaging Spectroradiometer (MODIS) visible to near-infrared reflectances); the gray diagonal line indicates the identity line. The number of observations (n), correlation coefficient r, and normalized root-mean-square deviation between τ_o^* and τ (nRMSD) is given. (b) PDF of the difference between τ and τ_o^*. (c) Same as (b) but for the cloud droplet number concentration (N and N_o^*). (d) Same as (a) but for the effective droplet radius (r_{eff} and $r_{eff,o}^*$). (e and f) Same as (b) but for liquid water path (LWP and LWP_o^*).

for PCL pixels, which were sampled above MBL clouds off the coast of California, can be reproduced for more complex broken cumulus fields from different locations.

7. MODIS PCL Data

MODIS VNIR and SWIR reflectances are reported at their native horizontal resolution of 250 and 500 m in the operational *MOD02QKM* and *MOD02HKM* files, respectively (these file names are reserved for the Terra platform; for Aqua the *MYD*-designation replaces *MOD*). Similar to the ASTER application before, in this section these subpixel observations are used to derive τ_o^*, $r_{eff,o}^*$, LWP_o^* and N_o^*. Since no MODIS cloud property retrievals are performed at the 250-m scale, in a first step the ratio of atmospherically corrected to uncorrected reflectance is determined for the necessary bands and applied to each of the 16 (for VNIR band observations) and 8 (for SWIR band observations) subpixels. Note, that atmospherically corrected reflectances at the pixel level scale of 1,000 m are reported in the operational *MOD06* level 2 files. Subsequently, the average cloudy reflectances are determined from Equation (1). Here, the pixel level reflectances $R_{0.86}$ and $R_{2.1}$ are the atmospherically corrected values provided by MODIS, while the average clear-sky reflectance is derived from the subpixel VNIR observations and the estimated C_{sub}^* and 250-m $R_{2.1}^*$. Also note, that only the respective $\approx 60 \times 60\,km^2$ ASTER scene is included in the MODIS analysis, that is, data are only from the respective subscene and not the whole MODIS granule. These subscenes are the colocated MODIS data set reported in

Werner et al. (2016). While ASTER does offer cross-track pointing capability, our data have all observations close to nadir, with viewing zenith angles ranging from 0.03° to 13.99°.

Compared to the ASTER analysis in this study, this test with MODIS data exhibits some inherent uncertainties: (i) The atmospheric correction based on 1,000-m data might be different from a theoretical 250-m result. (ii) The observational geometry of ASTER 960-m data and the operational MODIS results is different; not only due to the different pixel sizes but also because of different pixel orientations. This means that the retrieved cloud properties and calculated PCL biases might be noticeably different. (iii) For MODIS there is no ground truth to compare the retrieval results to. Consequently, the derived PCL biases are based on the difference between the retrieved cloud properties from the standard retrieval approach and the estimated results from the methods described in sections 4.1 and 4.2. Similarly, no operational C_{sub} is available, aside from the estimated values based on equation (2). As before, nearly clear or overcast pixels (i.e., very low and high C^*_{sub}) are excluded from the analysis. Here, the somewhat arbitrary thresholds of $C^*_{sub} = 3/16$ and $C^*_{sub} = 13/16$ are chosen, respectively, which yield a comparable number of PCL pixels as for the ASTER analysis.

Figure 12a shows a pixel level comparison between τ^*_o and τ, while Figure 12d illustrates a similar comparison between $r^*_{eff,o}$ and r_{eff}. Even though the reference retrievals are the respective estimated cloud properties, which are related to the overcast portion of a pixel, clear-sky contamination yields a similar underestimation of τ and general overestimation of r_{eff} for the MODIS observations (see Figure 4 for the ASTER comparison). The correlation coefficients are comparable to the ASTER analysis, whereas the nRMSD results are noticeably higher. Figures 12b and 12e show the respective PDFs of the relative difference between standard retrievals and the estimated, overcast results. For the cloud optical thickness, the 1st, 50th, and 99th percentiles of the relative difference $\tau - \tau^*_o$ are −65.06%, −25.24%, and −5.63% (absolute values of −3.70, −0.46, and −0.06), while statistics of −19.09%, 3.62%, and 68.00% (absolute values of −2.38, 0.39, and 8.72 μm) are observed for the difference $r_{eff} - r^*_{eff,o}$. These differences, as well as the observed distributions, are very similar to the ASTER biases reported in Table 3 and Figure 4, especially for the cloud optical thickness. Likewise, distributions for the difference $N - N^*_o$ and $LWP - LWP^*_o$ are shown in Figures 12c and 12f, respectively. The 1st, 50th, and 99th percentiles of each difference are −81.36%, −20.37%, and 39.13% (absolute values of −138.83, −8.39, and 22.78 cm^{-3}) for N and −61.69%, −22.83%, and 15.14% (absolute values of −26.73, −2.89, and 1.74 g/m^2) for LWP. While the maximum differences are rather different for both cloud parameters, the minimum and median biases are very similar to the ASTER PCL results (see Figure 10). Given the difficulties in comparing the two data sets and the lack of true reference retrievals, this good agreement confirms the improvements that can be achieved for PCL retrievals and a possible application for MODIS.

8. Summary and Conclusions

This study uses ASTER observations from MBL cloud scenes at different horizontal resolutions to evaluate cloud property retrievals for PCL pixels. It subsequently introduces techniques to estimate the subpixel cloud cover and reflectance distribution in the SWIR band by utilizing available subpixel observations of $R_{0.86}$ (in the VNIR). The high-resolution ASTER data provide the means to compare the pixel level results to reference retrievals, which are representative of the overcast part of a PCL pixel. As a result, this study conclusively illustrates that these estimates facilitate an improved cloud property retrieval for PCL pixels, which successfully mitigates the effects of clear-sky contamination. The approach can easily be adopted to similar MBL cloud observations from other imagers, such as MODIS, VIIRS, and SEVIRI.

ASTER measurements at a horizontal resolution of 30 m provide high-resolution cloud properties at the subpixel scale, while an aggregation of the observations to a scale of 960 m yields pixel level retrievals of τ and r_{eff}, which are comparable to the operational MODIS resolution. While the total reflectances $R_{0.86}$ and $R_{2.1}$ are comprised of clear-sky and overcast subpixel reflectances, averages of the subpixel reflectances from the overcast part yield the actual cloud properties τ_o and $r_{eff,o}$, which are unbiased by the clear-sky component of the PCL pixels. Naturally, for overcast pixels $\tau = \tau_o$ and $r_{eff} = r_{eff,o}$, but for PCL observations the pixel level retrievals of τ and r_{eff} can be severely biased. For the analyzed ASTER scenes in this study there are significant underestimations of τ and overestimations of r_{eff}, which can be larger than −58.46%) and 41.05% in magnitude, respectively. These biases directly impact the derivations of LWP and N, which both exhibit general underestimations of up to −68.37% and −72.00%, respectively. Due to the power laws involved in the calculations of N, biases can become as large as 104%. Note that these quantitative results are specific to the studied data set and are not necessarily expected for other observations (e.g., global MODIS retrievals).

To mitigate the impact of clear-sky contamination for PCL pixels, methods to estimate C^*_{sub} and $R^*_{2.1}$ at a horizontal subpixel resolution of 240 m are introduced, which are based on the availability of high-resolution $R_{0.86}$ observations. The derivation of C^*_{sub} follows the operational MODIS approach and a comparison between the results and the actually observed C_{sub} reveals a good agreement with a high correlation. Meanwhile, estimates of $R^*_{2.1}$ are subject to different assumptions about the subpixel cloud characteristics. Of the three proposed assumptions, the Constant Reflectance Ratio Approach yields a good comparison between $R^*_{2.1}$ and the observed $R_{2.1}$ for PCL pixels, while remaining independent of a successful pixel level retrieval and computationally efficient. The described methods provide the necessary estimates of the average cloudy subpixel reflectance for the retrieval of τ^*_o and $r^*_{eff,o}$, which agree well with the actually observed cloud properties. The remaining mean biases for both results are greatly reduced, from −17.01% to −0.45% (for τ and τ^*_o) and from 6% to −0.56% (for r_{eff}, and $r^*_{eff,o}$). Similar improvements compared to the standard results are achieved for the derived parameters LWP^*_o and N^*_o, where remaining mean biases are −1.72% (down from −18.67%) and 0.77% (down from −18.41%), respectively.

The assumptions to estimate C^*_{sub} and $R^*_{2.1}$, as well as the reliability of the improved PCL retrieval, are evaluated by means of an extended ASTER data set. These additional MBL cloud fields are composed of broken cumulus and are significantly more complex. They are characterized by small horizontal cloud diameters and low scene cloud covers, as well as the occurrence of sun glint and land surfaces. However, the retrieved τ^*_o, $r^*_{eff,o}$, LWP^*_o, and N^*_o still agree well with the actually observed cloud properties and the impact of clear-sky contamination can be successfully mitigated. Considering that C^*_{sub} is already provided by the operational MODIS C6 cloud product, implementation of a PCL retrieval following those estimations and equation (1) for all cloudy MODIS pixels appears to be feasible and would likely result in an improved cloud property retrieval for MBL cloud scenes.

While for MODIS observations there is neither an operational C_{sub} nor the necessary reference retrievals for an evaluation, an application of the proposed PCL retrieval scheme still allows for an analysis of retrieval biases due to clear-sky contamination, similar to the ASTER analysis. Here the subpixel VNIR and SWIR reflectances are provided by the MODIS level-1 samples at horizontal resolutions of 250 m and 500 m, respectively. A comparison between the operational retrievals results at the native 1,000 m scale and the estimated values τ^*_o and $r^*_{eff,o}$ yields underestimations of > 3.00 and overestimations of > 8 μm, respectively. Despite different observational geometries, the derived bias distributions and median biases are similar to the ASTER results.

It is important to note that the proposed PCL retrieval approach has only been tested and evaluate for MBL clouds, where there is sufficient contrast between the bright cloud tops and the dark ocean surface. It is reasonable to assume that the reliability of the retrieved cloud products suffers for more complex cloud fields, primarily due to uncertainties in C^*_{sub}. The simple cloud masking scheme based on high-resolution observations at VNIR bands will likely yield substantial overestimations of C^*_{sub} if the sampled scenes exhibit an increased aerosol particle loading, overlying cirrus, sunglint or strong radiative smoothing as a consequence of 3-D radiative effects (i.e., low solar zenith angles and horizontal photon transport). Similarly, estimates of C^*_{sub} that are only determined by the $R_{0.86}$ threshold are subject to possible false cloud classifications on the subpixel scale for measurements over bright surfaces (e.g., sand and urban landscapes). However, given that the standard retrieval for PCL pixels assumes that $C_{sub} = 1$, a slight overestimation of C^*_{sub} would still signify an improvement, while a worst-case scenario ($C^*_{sub} = C_{sub} = 1$) would provide identical results (i.e., $\tau^*_o = \tau$; similar for the other cloud properties).

Not discussed in this study is the possibility of reducing the number of failed PCL retrievals. About 36.81% of all PCL observations for the data set in section 6 exhibit failed retrievals, predominantly because $R_{2.1}$ becomes too low. The removal of the clear-sky component yields a successful τ_o and $r_{eff,o}$ retrieval for 87.65% for these pixels. Additionally, equation (1 also helps to identify 14.44% of clear pixel level observations as PCL ones (i.e., a clear 960 − m pixel includes at least one cloudy 240-m subpixel). Also not discussed are biases due to the plane-parallel homogeneous bias. While the mathematical framework presented in Zhang et al. (2016) is shown to successfully mitigate observed retrieval biases, it is only suitable for overcast conditions (Werner et al., 2018). Since this study provides the means to derive the average cloudy reflectance and respective cloud properties, a correction of the plane-parallel homogeneous bias can now also be applied to PCL pixels, which improves the reliability even further. At last, it is important to note that the retrieved τ_o and $r_{eff,o}$

might be impacted by 3-D radiative effects. PCL pixels are more susceptible to biases induced by unaccounted horizontal photon transport, especially for observations with low C_{sub}. These issues will be studied in future works.

Acknowledgments
This study is supported by NASA grants NNX14AJ25G and NNX15AC77G. The hardware used in the computational studies is part of the UMBC High Performance Computing Facility (HPCF). The facility is supported by the U.S. National Science Foundation through the MRI program (grants CNS-0821258 and CNS-1228778) and the SCREMS program (grant DMS-0821311), with additional substantial support from the University of Maryland, Baltimore County (UMBC). ASTER data are obtained by the EarthExplorer interface (http://earthexplorer.usgs.gov) provided by the U.S. Geological Survey (USGS). ASTER cloud property retrievals are based on a research level retrieval algorithm and a publicly available, quality-assured product is in preparation. In the meantime, we have a preliminary data set of cloud top, optical, and microphysical properties, as well as cloud masking information, for several hundred marine stratocumulus and broken cumulus scenes sampled by ASTER (Werner et al., 2016; Zhao et al., 2009). We are happy to share these products with the community and encourage anybody interested in the data, which are available in HDF4 format, to contact us (either frankw@umbc.edu or zzbatmos@umbc.edu). Zhibo Zhang's research is partly supported by the U.S. Department of Energy (DOE), Office of Science, Biological and Environmental Research, Regional and Global Climate Modeling Program (grant DE-SC0014641).

References

Abrams, M. (2000). The advanced spaceborne thermal emission and reflection radiometer (ASTER): Data products for the high spatial resolution imager on NASA's Terra platform. *International Journal of Remote Sensing*, *21*(5), 847–859.

Abrams, M., Hook, S., & Ramachandran, B. (2004). *ASTER user handbook version 2*. Pasadena, CA 91109: Jet Propulsion Laboratory, California Institute of Technology, 4800 Oak Grove Dr.

Ackerman, S. A., Holz, R. E., Frey, R., Eloranta, E. W., Maddux, B. C., & McGill, M. (2008). Cloud detection with MODIS. Part II: Validation. *Journal of Atmospheric and Oceanic Technology*, *25*, 1073–1086. https://doi.org/10.1175/2007JTECHA1053.1

Ackerman, S. A., Strabala, K. I., Menzel, W. P., Frey, R. A., Moeller, C. C., & Gumley, L. E. (1998). Discriminating clear sky from clouds with MODIS. *Journal of Geophysical Research*, *103*, 32,141–32,157.

Ackerman, A., Toon, O., Taylor, J., Johnson, D., Hobbs, P., & Ferek, R. (2000). Effects of aerosols on cloud albedo: Evaluation of Twomey's parameterization of cloud susceptibility using measurements of ship tracks. *Journal of the Atmospheric Sciences*, *57*, 2684–2695.

Albrecht, B. A. (1989). Aerosols, cloud microphysics, and fractional cloudiness. *Science*, *245*(4923), 1227–1230.

Arking, A., & Childs, J. D. (1985). Retrieval of cloud cover parameters from multispectral satellite images. *Journal of Climate and Applied Meteorology*, *24*, 322–333.

Barker, H., & Liu, D. (1995). Inferring optical depth of broken clouds from Landsat data. *Journal of Climate*, *8*, 2620–2630.

Baum, B. A., Menzel, W. P., Frey, R. A., Tobin, D., Holz, R. E., Ackerman, S. A., et al. (2012). Modis cloud–top property refinements for collection 6. *Journal of Applied Meteorology and Climatology*, *51*, 1145–1163. https://doi.org/10.1175/JAMC-D-11-0203.1

Bennartz, R. (2007). Global assessment of marine boundary layer cloud droplet number concentration from satellite. *Journal of Geophysical Research*, *112*, D02201. https://doi.org/10.1029/2006JD007547

Boeke, R. C., Allan, A. M., & Coakley, J. A. (2016). Properties of marine stratocumulus obtained with partly cloudy pixel retrievals and found in the MODIS MOD06 cloud product. *Journal of Geophysical Research: Atmospheres*, *121*, 6404–6424. https://doi.org/10.1002/2015JD024149

Brenguier, J.-L., Pawlowska, H., Schüller, L., Preusker, R., Fischer, J., & Fouquart, Y. (2000). Radiative properties of boundary layer clouds: Droplet effective radius versus number concentration. *Journal of the Atmospheric Sciences*, *57*(7), 803–821.

Chambers, L., Wielicki, B., & Evans, K. (1997). Accuracy of the independent pixel approximation for satellite estimates of oceanic boundary layer cloud optical depth. *Journal of Geophysical Research*, *102*, 1779–1794.

Cho, H.-M., Zhang, Z., Meyer, K., Lebsock, M., Platnick, S., Ackerman, A. S., et al. (2015). Frequency and causes of failed modis cloud property retrievals for liquid phase clouds over global oceans. *Journal of Geophysical Research: Atmospheres*, *120*, 4132–4154. https://doi.org/10.1002/2015JD023161

Coakley, J. A., Friedman, M. A., & Tahnk, W. R. (2005). Retrieval of cloud properties for partly cloudy imager pixels. *Journal of Atmospheric and Oceanic Technology*, *22*(1), 3–17. https://doi.org/10.1175/JTECH-1681.1

Dey, L., Di Girolamo, L., & Zhao, G. (2008). Scale effect on statistics of the macrophysical properties of trade wind cumuli over the tropical western Atlantic during RICO. *Journal of Geophysical Research*, *113*, D24214. https://doi.org/10.1029/2008JD010295

Di Girolamo, L., & Davies, R. (1997). Cloud fraction errors caused by finite resolution measurements. *Journal of Geophysical Research*, *102*(D2), 1739–1756.

Di Girolamo, L., Liang, L., & Platnick, S. (2010). A global view of one-dimensional solar radiative transfer through oceanic water clouds. *Geophysical Research Letters*, *37*, L18809. https://doi.org/10.1029/2010GL044094

Feingold, G., Koren, I., Wang, H. L., Xue, H. W., & Brewer, W. A. (2010). Precipitation-generated oscillations in open cellular cloud fields. *Nature*, *466*(7308), 849–852. https://doi.org/10.1038/nature09314

Han, Q., Rossow, W., & Lacis, A. (1994). Near-global survey of effective droplet radii in liquid water clouds using ISCCP data. *Journal of Climate*, *7*, 465–497.

Hayes, C. R., Coakley, J. A., & Tahnk, W. R. (2010). Relationships among properties of marine stratocumulus derived from collocated CALIPSO and MODIS observations. *Journal of Geophysical Research*, *115*, D00H17. https://doi.org/10.1029/2009JD012046

King, M. D., Platnick, S., Wenzel, W. P., Ackerman, S. A., & Hubanks, P. A. (2013). Spatial and temporal distribution of clouds observed by MODIS onboard the Terra and Aqua satellites. *IEEE Transactions on Geoscience and Remote Sensing*, *51*(7), 3826–3852. https://doi.org/10.1109/TGRS.2012.2227333

King, M. D., Tsay, S.-C., Platnick, S. E., & Liou, K.-N. (1997). Cloud retrieval algorithms for MODIS: Optical thickness, effective particle radius, and thermodynamic phase. MODIS Algorithm Theoretical Basis Document ATBD-MOD-05, NASA (78 pp.).

Klein, S., & Hartmann, D. (1993). The seasonal cycle of low stratiform clouds. *Journal of Climate*, *6*, 1587–1606.

Krijger, J. M., van Weele, M., Aben, I., & Frey, R. (2007). Technical note: The effect of sensor resolution on the number of cloud-free observations from space. *Atmospheric Chemistry and Physics*, *7*, 2881–2891.

Liang, L. S., Di Girolamo, L., & Platnick, S. (2009). View-angle consistency in reflectance, optical thickness and spherical albedo of marine water-clouds over the northeastern pacific through MISR-MODIS fusion. *Geophysical Research Letters*, *36*, L09811. https://doi.org/10.1029/2008GL037124

Lohmann, U., Rotstayn, L., Storelvmo, T., Jones, A., Menon, S., Quaas, J., et al. (2010). Total aerosol effect: Radiative forcing or radiative flux perturbation? *Atmospheric Chemistry and Physics*, *10*(7), 3235–3246.

Marshak, A., Platnick, S., Varnai, T., Wen, G. Y., & Cahalan, R. F. (2006). Impact of three-dimensional radiative effects on satellite retrievals of cloud droplet sizes. *Journal of Geophysical Research*, *111*, D09207. https://doi.org/10.1029/2005JD006686

Miller, D. J., Zhang, Z., Ackerman, A. S., Platnick, S., & Baum, B. A. (2016). The impact of cloud vertical profile on liquid water path retrieval based on the bispectral method: A theoretical study based on large-eddy simulations of shallow marine boundary layer clouds. *Journal of Geophysical Research: Atmospheres*, *121*, 4122–4141. https://doi.org/10.1002/2015JD024322

Minnis, P., Harrison, E. F., & Gibson, G. G. (1987). Cloud cover over the equatorial eastern pacific derived from July 1983 international satellite cloud climatology project data using a hybrid bispectral threshold method. *Journal of Geophysical Research*, *92*(D4), 4051–4073. https://doi.org/10.1029/JD092iD04p04051

Nakajima, T., & King, M. (1990). Determination of the optical thickness and effective particle radius of clouds from reflected solar radiation measurements. Part I: Theory. *Journal of the Atmospheric Sciences*, *47*, 1878–1893.

Nakajima, T., King, M., Spinhirne, J., & Radke, L. (1991). Determination of the optical thickness and effective particle radius of clouds from reflected solar radiation measurements. Part II: Marine stratocumulus observations. *Journal of the Atmospheric Sciences*, *48*, 728–750.

Norris, J. (1999). On trends and possible artifacts in global ocean cloud cover between 1952 and 1995. *Journal of Climate*, *12*, 1864–1870.
Platnick, S., King, M., Ackerman, S., Menzel, W., Baum, B., Riedi, J., & Frey, R. (2003). The MODIS cloud products: Algorithms and examples from Terra. *IEEE Transactions on Geoscience and Remote Sensing*, *41*, 459–473.
Quaas, J., Boucher, O., & Lohmann, U. (2006). Constraining the total aerosol indirect effect in the LMDZ and ECHAM4 GCMs using MODIS satellite data. *Atmospheric Chemistry and Physics*, *6*(4), 947–955. https://doi.org/10.5194/acp-6-947-2006
Ramaswamy, V., & Chen, C.-T. (1993). An investigation of the global solar radiative forcing due to changes in cloud liquid water path. *Journal of Geophysical Research*, *98*(D9), 16,703–16,712. https://doi.org/10.1029/93JD01282
Rauber, R. M., Stevens, B., Ochs III, H. T., Knight, C., Albrecht, B. A., Blyth, A. M., et al. (2007). Rain in shallow cumulus over the ocean: The RICO campaign. *Bulletin of the American Meteorological Society*, *88*(12), 1912–1928. https://doi.org/10.1175/BAMS-88-12-1912
Schmeissner, T., Shaw, R. A., Ditas, J., Stratmann, F., Wendisch, M., & Siebert, H. (2015). Turbulent mixing in shallow trade wind cumuli: Dependence on cloud life cycle. *Journal of the Atmospheric Sciences*, *72*(4), 1447–1465. https://doi.org/10.1175/JAS-D-14-0230.1
Schüller, L., Bennartz, R., Fischer, J., & Brenguier, J.-L. (2005). An algorithm for the retrieval of droplet number concentration and geometrical thickness of stratiform marine boundary layer clouds applied to MODIS radiometric observations. *Journal of Applied Meteorology*, *44*(1), 28–38. https://doi.org/10.1175/JAM-2185.1
Seifert, A., Heus, T., Pincus, R., & Stevens, B. (2015). Large-eddy simulation of the transient and near-equilibrium behavior of precipitating shallow convection. *Journal of Advances in Modeling Earth Systems*, *7*, 1918–1937. https://doi.org/10.1002/2015MS000489
Shenk, W., & Salomonson, V. (1972). A simulation study exploring the effects of sensor spatial resolution on estimates of cloud cover from satellite. *Journal of Applied Meteorology*, *11*, 214–220.
Siebert, H., Bethke, J., Bierwirth, E., Conrath, T., Dieckmann, K., Ditas, F., et al. (2013). The fine–scale structure of the trade wind cumuli over Barbados – an introduction to the CARRIBA project. *Atmospheric Chemistry and Physics*, *13*, 10,061–10,077. https://doi.org/10.5194/acp-13-10061-2013
Stevens, B., Vali, G., Comstock, K., Wood, R., van Zanten, M. C., Austin, P. H., et al. (2005). Pockets of open cells and drizzle in marine stratocumulus. *Bulletin of the American Meteorological Society*, *86*(1), 51–58. https://doi.org/10.1175/BAMS-86-1-51
Tiedtke, M. (1989). A comprehensive mass flux scheme for cumulus parameterization in large-scale models. *Monthly Weather Review*, *117*(8), 1779–1800. https://doi.org/10.1175/1520-0493(1989)117<1779:ACMFSF>2.0.CO;2
Twomey, S. (1974). Pollution and the planetary albedo. *Atmospheric Environment*, *8*, 1251–1256.
Twomey, S. (1977). The influence of pollution on the shortwave albedo of clouds. *Journal of the Atmospheric Sciences*, *34*, 1149–1152.
Twomey, S., & Seton, K. J. (1980). Inferences of gross microphysical properties of clouds from spectral reflectance measurements. *Journal of the Atmospheric Sciences*, *37*(5), 1065–1069.
Warren, S., Hahn, C., London, J., Chervin, R., & Jenne, R. (1988). Global distribution of total cloud cover and cloud type amounts over the ocean (Tech. Rep) Boulder, CO: National Center for Atmospheric Research.
Werner, F., Ditas, F., Siebert, H., Simmel, M., Wehner, B., Pilewskie, P., et al. (2014). Twomey effect observed from collocated microphysical and remote sensing measurements over shallow cumulus. *Journal of Geophysical Research: Atmospheres*, *119*, 1534–1545. https://doi.org/10.1002/2013JD020131
Werner, F., Wind, G., Zhang, Z., Platnick, S., Di Girolamo, L., Zhao, G., et al. (2016). Marine boundary layer cloud property retrievals from high-resolution ASTER observations: Case studies and comparison with Terra MODIS. *Atmospheric Measurement Techniques*, *9*(12), 5869–5894. https://doi.org/10.5194/amt-9-5869-2016
Werner, F., Zhang, Z., Wind, G., Miller, D. J., & Platnick, S. (2018). Quantifying the impacts of subpixel reflectance variability on cloud optical thickness and effective radius retrievals based on high–resolution ASTER observations. *Journal of Geophysical Research: Atmospheres*, *123*, 4239–4258. https://doi.org/10.1002/2017JD027916
Wielicki, B. A., & Parker, L. (1992). On the determination of cloud cover from satellite sensors: The effect of sensor spatial resolution. *Journal of Geophysical Research*, *97*(D12), 12,799–12,823.
Wood, R. (2012). Stratocumulus clouds. *Monthly Weather Review*, *140*(8), 2373–2423. https://doi.org/10.1175/MWR-D-11-00121.1
Wood, R., Comstock, K. K., Bretherton, C. S., Cornish, C., Tomlinson, J., Collins, D. R., & Fairall, C. (2008). Open cellular structure in marine stratocumulus sheets. *Journal of Geophysical Research*, *113*, D12207. https://doi.org/10.1029/2007JD009371
Wood, R., & Hartmann, D. L. (2006). Spatial variability of liquid water path in marine low cloud: The importance of mesoscale cellular convection. *Journal of Climate*, *19*(9), 1748–1764.
Yamaguchi, Y., Kahle, A., Tsu, H., Kawakami, T., & Pniel, M. (1998). Overview of advanced spaceborne thermal emission and reflection radiometer (ASTER). *IEEE Transactions on Geoscience and Remote Sensing*, *36*, 1062–1071.
Yamaguchi, Y., Tsu, H., & Fujisada, H. (1993). Scientific basis of ASTER instrument design. *Proceedings of SPIE*, *1939*, 150–160. https://doi.org/10.1117/12.152841
Yang, Y., & Di Girolamo, L. (2008). Impacts of 3-D radiative effects on satellite cloud detection and their consequences on cloud fraction and aerosol optical depth retrievals. *Journal of Geophysical Research*, *113*, D04213. https://doi.org/10.1029/2007JD009095
Zhang, Z., Ackerman, A. S., Feingold, G., Platnick, S., Pincus, R., & Xue, H. (2012). Effects of cloud horizontal inhomogeneity and drizzle on remote sensing of cloud droplet effective radius: Case studies based on large-eddy simulations. *Journal of Geophysical Research*, *117*, D19208. https://doi.org/10.1029/2012JD017655
Zhang, Z., & Platnick, S. (2011). An assessment of differences between cloud effective particle radius retrievals for marine water clouds from three MODIS spectral bands. *Journal of Geophysical Research*, *116*, D20215. https://doi.org/10.1029/2011JD016216
Zhang, Z., Werner, F., Cho, H.-M., Wind, G., Platnick, S., Ackerman, A. S., et al. (2016). A framework based on 2-D Taylor expansion for quantifying the impacts of subpixel reflectance variance and covariance on cloud optical thickness and effective radius retrievals based on the bispectral method. *Journal of Geophysical Research: Atmospheres*, *121*, 7007–7025. https://doi.org/10.1002/2016JD024837
Zhao, G., & Di Girolamo, L. (2006). Cloud fraction errors for trade wind cumuli from EOS-terra instruments. *Geophysical Research Letters*, *33*, L20802. https://doi.org/10.1029/2006GL027088
Zhao, G., & Di Girolamo, L. (2007). Statistics on the macrophysical properties of trade wind cumuli over the tropical western Atlantic. *Journal of Geophysical Research*, *112*, D10204. https://doi.org/10.1029/2006JD007371
Zhao, G., Di Girolamo, L., Dey, S., Jones, A. L., & Bull, M. (2009). Examination of direct cumulus contamination on MISR-retrieved aerosol optical depth and angstrom coefficient over ocean. *Geophysical Research Letters*, *36*, L13811. https://doi.org/10.1029/2009GL038549